Mechanism of Corrosion of Cast Aluminum-Silicon Alloys in Seawater. Part 1: Characterization and Field Testing of Bare Alloys in the Adriatic Sea

Ingrid Milošev,[†,] Barbara Kapun,[*] Peter Rodič,[*] Charly Carrière,[**] Dimitri Mercier,[**] Sandrine Zanna,[**] and Philippe Marcus[†,**]*

Aluminum-silicon cast alloys are increasingly used in various applications, including marine. Two Al-Si cast alloys were investigated as materials for marine exposure: Al-Si9-Cu3 and Al-Si7-Mg0.3. Microstructure, chemical composition, and electrochemical properties of nonimmersed alloys were studied, revealing their heterogeneous nature. Eight months of field testing by immersion in the Adriatic Sea was performed to test long-term corrosion and biofouling resistance. Morphological and chemical changes at the surface induced by immersion were investigated using surface analytical techniques. Top and cross-section surfaces were investigated. Electrochemical measurements of immersed samples in artificial seawater revealed that alloys were re-passivated by micrometer-thick oxide layers. Al-Si9-Cu3 alloy forms a layer rich in magnesium, while that formed on Al-Si7-Mg0.3 is rich in silicon. Electrochemical results indicate that both alloys are suitable for use in marine environments, where Al-Si7-Mg0.3 is more resistant than Al-Si9-Cu3. Biofouling formed up to one month of immersion can be removed by sonication. At the end of the immersion period, macro biofouling was firmly attached to the alloys' surface, as evidenced by scanning electron microscopy.

KEY WORDS: aluminum-silicon cast alloys, field testing, focused ion beam/scanning electron microscopy/energy dispersive x-ray spectroscopy, glow discharge optical emission spectroscopy, marine immersion, x-ray photoelectron spectroscopy

INTRODUCTION

Aluminum alloys are used in transportation due to their low weight (density 2.71 g/dm^3) and suitable mechanical properties. For marine applications, both wrought and cast alloys are being used. Among wrought alloys, those of series 5xxx (Al-Mg, i.e., AA5083, 5086, 5754) and 6xxx (Al-Mg-Si, e.g., AA6082, 6061, 6063) are suitable for their ease of assembly by welding and excellent corrosion resistance.[1-3] These alloys are used for marine structural applications such as hull structures, superstructures, decks, etc. Nonheat treatable alloys of series 5xxx belong to strain hardening alloys manufactured by a sequence of hot, then cold, forming operations (rolling for sheets) combined with intermediate and final annealing.[4] By adding Mg (and Mn), cold work and solid solution strengthening contribute to alloys' strength, high corrosion resistance, and toughness. Alloys of series 6xxx containing Mg and Si are age-hardening alloys that obtain their mechanical properties through solution heat treatment at high temperatures, followed by quenching and natural or artificial aging. During the latter phase, the alloying elements form fine, dispersed precipitates that increase the metal's hardness. The formation of Mg_2Si provides these alloys with heat-treatability.[1] Alloys of series 6xxx, complementary to the 5xxx series, are easily machinable into various shapes and forms by rolling, extrusion, and forging.[1,4]

Due to their structural integrity, enhanced mechanical properties, and other properties, wrought alloys account for around 63% of total sales of aluminum alloys.[5] However, the use of cast aluminum alloys has grown in recent years mainly because of their good castability and high specific strength. Compared with wrought Al alloys, casting alloys have clear economic advantages due to their shorter processing cycle and assembly costs.[6] Therefore, market demands are high, and the need for aluminum alloys with good material properties is increasing. The 40000 (Al-Si) and 50000 (Al-Mg) series according to EN AC[(1)] are used in marine applications.[1,7] Alloys of series 40000 have excellent potential for casting components of complex shapes, very good weldability, and mechanical properties. They are used for ship superstructures, structural components, interior fitments, assemblies with mechanical functions, etc. The addition of silicon to aluminum reduces melting temperature and improves fluidity.[1]

According to the Al-Si phase diagram, at room temperature, the solubility of Si in Al is very low.[8] The eutectic

Submitted for publication: September 15, 2022. Revised and accepted: December 30, 2022. Preprint available online: December 30, 2022, https://doi.org/10.5006/4205.
[‡] Corresponding authors. E-mail: ingrid.milosev@ijs.si; philippe.marcus@chimieparistech.psl.eu.
[*] Jožef Stefan Institute, Department of Physical and Organic Chemistry, Jamova c. 39, Ljubljana, 1000, Slovenia.
[**] CNRS—Chimie ParisTech, PSL University, Institut de Recherche de Chimie Paris, Physical Chemistry of Surfaces Group, 11 rue Pierre et Marie Curie, Paris, 75005, France.
[(1)] EN = European Standards (German "Europäische Norm" EN), AC = Aluminum Cast.

ISSN 0010-9312 (print), 1938-159X (online)

temperature is 577°C, and the eutectic composition is 12.7% silicon. Depending on the Si content, these alloys are regarded as hypo-eutectic (5% to 11%), eutectic (12.6 wt%), and hyper-eutectic (13 wt% to 23 wt%). The hypoeutectic Al-Si casting alloys exhibit suitable castability, weldability, low thermal expansion coefficient, good corrosion resistance, and machinability.[1,9] The most significant disadvantage of Al-Si alloys is the lack of heat-treatment capability.[10] For that reason, Mg is added, which forms the secondary-phase precipitates Mg_2Si and Mg-rich intermetallics.[1,10-11] Cu is often added to increase the strength by forming the intermetallic phase Al_2Cu.[1] Copper significantly decreases the solidus and eutectic temperatures and, therefore, enlarges the solidification interval of an alloy.

During solidification, the microstructure evolves in two stages: primary dendrite Al-phase formation (α-Al-rich matrix) and the subsequent eutectic transformation (eutectic Si particles in α-matrix). The volume fraction of Al-Si eutectic in commonly used hypoeutectic Al-Si alloys, such as Al-Si7-Mg0.3, Al-Si9-Cu3, and Al-Si6-Cu4, can be more than 50%.[9] Primary alloying elements are not completely soluble in the α-Al matrix and sometimes combine with impurities and matrix to form intermediate (intermetallic) phases,[11] among which are Fe-based, i.e., Al(Fe,Mn)Si,[12-13] two most important being α-phase ("Chinese scripts") and β-phase (needle or plates), and ε-Mg_2Si. In addition, Cu-containing intermetallic particles (IMPs) such as θ-Al_2Cu and Q-$Al_5Cu_2Mg_8Si$ also form.[14-16] All of these IMPs and eutectic-Si are noble to the α-Al matrix except Mg_2Si, which is less noble.

Aluminum alloys used in marine applications are subject to different types of corrosion, the most important being pitting, trans- and intergranular corrosion, crevice, and exfoliation corrosion.[1,4] Alloys containing more than 3 wt% Mg become susceptible to intergranular corrosion (IGC) when exposed to temperatures as low as 50°C over long periods.[17] IGC can lead to mass loss (through grain fall-out) and intergranular stress corrosion cracking in the presence of stress.[18] Intercrystalline corrosion is caused by the difference in electrochemical potential between the actual grain and the grain boundary zone where intermetallic compounds, such as the β-Al_3Mg_2 phase for magnesium alloys, can precipitate.[17-18]

There are several reports on the electrochemical and corrosion behavior of cast Al-Si alloys. Hypoeutectic aluminum-silicon alloys Al-Si5 and Al-Si9 were studied in 0.5 M NaCl; the increased Si content resulted in a dendritic refinement and a more extensive distribution of the eutectic region with a deleterious effect on the corrosion resistance.[19] The addition of eutectic modifier (commercial flux containing mainly sodium fluoride), which promotes the improvement of mechanical properties, harmed the corrosion properties of Al-Si9 that was ascribed to an increase in boundaries between the Al-rich phase and Si particles growth during the melt.[20] Si particles disseminated through Al-rich phase should make the alloy more susceptible to corrosion since Si is nobler than Al.[20] However, the effects of silicon on the corrosion resistance of Al-Si-based casting alloys are minimal because of low corrosion current density resulting from the fact that the silicon particles are highly polarized.[1] The protectivity of the Al-12%Si alloy in borate buffer (pH 8.4) containing 0.01 M NaCl was partly attributed to its ability to retard the adsorption of chloride ion, as concluded based on double-layer capacitance measurements.[21] Namely, the difference between the potential of zero charge and corrosion potential was negative (−61 mV), reflecting a smaller susceptibility to pitting. It was concluded that silicon oxide helps blocking entry sites and restricts the transport of chloride ions through the passive film.[21] The effect of the casting procedure of hypoeutectic Al-Si alloy was studied in different chloride concentrations.[22] No significant difference in casting procedure on the corrosion behavior was noticed. The mechanism of corrosion was shown to proceed in three steps: (i) initiation of microgalvanic corrosion at Al/Fe-rich intermetallic particle interface, (ii) progression of corrosion inside eutectic regions, and (iii) precipitation of corrosion products—the gel (dry mud)-like layer in the center of corrosion process of cathodically active sites and fine powdery corrosion products at the surrounding sites of lower pH.[22]

The corrosion resistance of a series of hypoeutectic alloys was investigated in 0.6 M NaCl.[23] All alloys exhibited good corrosion resistance; those with higher Cu and Si content had more positive corrosion potential. Al-Si7-Mg0.3 exhibited the lowest corrosion current density and more negative corrosion potential than Al-Si9-Cu3 alloy.[23] Similar behavior of hypo- and hypereutectic Al-Si alloys in 0.5 M NaCl was noticed, but the latter exhibited a lower corrosion current density.[24] Corrosion behavior of cast Al-Si alloys in NaCl solution was improved by adding rare earth elements.[25]

Several papers reported that the oxide film formed in chloride-containing solution is affected by the presence of alloying elements. It seems, however, that the detailed examination of the composition, structure, and electrochemical properties of hypoeutectic cast Al-Si alloys is still missing. Further, the characterization of these alloys during long-term immersion in seawater will bring some novel data on corrosion mechanisms during field exposure. In this study, we focus on two cast alloys: EN AC[(1)] 42100 (Al-Si7-Mg0.3) and EN AC 46000 (Al-Si9-Cu3(Fe)). Our previous studies dealt with these alloys in terms of their protection using zirconium conversion coatings.[26-28] For Al-Si7-Mg0.3, we studied its corrosion behavior in artificial seawater in the presence of sodium sulfide.[29] The surface-analytical analysis of metals exposed to artificial seawater and bacteria was explored in our previous studies on stainless steel.[30-31] This study investigated the microstructure, composition, and electrochemical corrosion characteristics of bare and coated Al-Si9-Cu3 and Al-Si7-Mg0.3 alloys. The microstructure and composition were investigated using focused ion beam scanning electron microscopy (FIB-SEM) with energy dispersive x-ray spectroscopy (EDS), x-ray photoelectron spectroscopy (XPS), and glow discharge optical emission spectroscopy (GDOES). In Part 1 of the series, we investigated the bare alloys before and after immersion in seawater. In Part 2 of the series, we investigated the coated Al-Si9-Cu3 and Al-Si7-Mg0.3 alloys before and after immersion in seawater.[32] Two types of sol-gel coatings synthesized in our laboratory were applied as coatings. Field immersion testing was performed in the Adriatic Sea. The antifouling performance was qualitatively determined using sonication to remove the biofouling attached to the surface.

EXPERIMENTAL PROCEDURES

2.1 | Substrate Materials

Two types of aluminum alloys were manufactured by Talum d.d. Kidričevo, Slovenia, and used as substrates (Table 1): (1) Al-Si9-Cu3 alloy (380.0/EN AC[(1)] 46000/EN AC Al-Si9-Cu3 (Fe)/UNS[(2)] A0380) and (2) Al-Si7-Mg0.3 alloy (A356.0/EN AC 42100/EN AC Al-Si7-Mg0.3/UNS A13560).

[(2)] UNS numbers are listed in *Metals & Alloys in the Unified Numbering System*, published by the Society of Automotive Engineers (SAE International) and cosponsored by ASTM International.

Table 1. *The Composition of Al-Si9-Cu3 and Al-Si7-Mg0.3 Cast Alloys Manufactured by Talum d.d., Kidričevo, Slovenia.*

Alloy	Composition (wt%)										
	Si	Mg	Fe	Cu	Mn	Zn	Ti	Cr	Ni	Pb	Sn
Al-Si9-Cu3	8.0–11.5	0.15–0.55	0.6–1.1	2.0–4.0	0.55	1.2	0.20	0.15	0.55	0.35	0.25
Al-Si7-Mg0.3	6.5–7.5	0.30–0.45	0.15	0.03	0.10	0.07	0.18	–	–	–	–

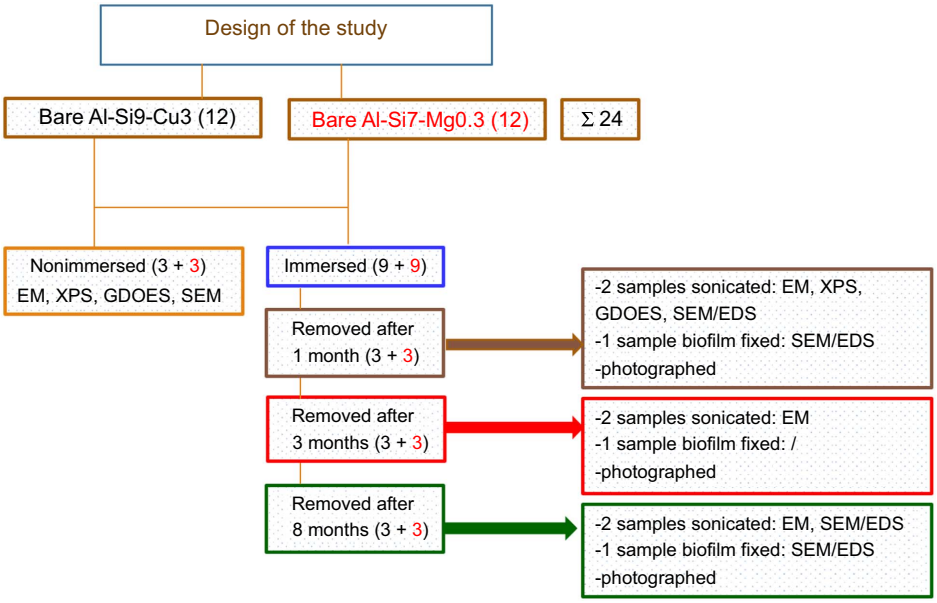

FIGURE 1. *Organigram presents the design of the study. EM: electrochemical measurements; XPS; SEM; and GDOES. The numbers of samples are given in parentheses.*

Samples were cut in the form of plates with dimensions 80 mm × 39 mm × 4 mm (Al-Si9-Cu3) and 80 mm × 34 mm × 4 mm (Al-Si7-Mg0.3). On each shorter side of the rectangle, a hole with a diameter of 3 mm was made to fix the sample on the rack using a plastic string. Samples were then water-ground on both sides using SiC emery paper of 320-grit (LabPole-5†, Struers, Ballerup, Denmark). Twenty-four bare samples were prepared (12 of each alloy type, Figure 1).

For SEM/EDS analysis, the nonimmersed samples were water-ground successively using SiC-paper up to 4000 grit.

2.2 | Design of the Study

2.2.1 | Preparation of the Samples

Out of each set of 12 bare samples, three were used as benchmarks for the characterization before the immersion in the Adriatic Sea (Figure 1). Electrochemical measurements, XPS, GDOES, and SEM analyses were performed on these samples. Nine bare samples of each alloy type were immersed in the Adriatic Sea, with three replicates for each immersion period (1, 3, and 8 months).

Samples were mounted on a specially designed rack (Figure 2[b]) made of polypropylene, which carried 12 samples. Samples were fixed to the rack using a plastic string fastened through the hole made on the sample (Figure 2[a]). Racks with samples were then fixed to a specially designed frame (Figure 2[b]). Each rack carried the samples to be removed simultaneously, so after the designated immersion period, the diver removed the whole rack from the sea. This arrangement avoided removing individual samples from the rack, which is not easy while samples were immersed deep below sea level. Samples were taken out after 1, 3, and 8 months.

2.2.2 | Field Testing in the Adriatic Sea

The immersion of the samples was performed in collaboration with the Marine Biology Station (MBS) of the National Institute of Biology in Piran, Slovenia. The MBS infrastructural center operates a research vessel (12 m), a boat (5 m), and a diving base with SCUBA facilities. Oceanographic buoy Vida provides real-time meteorological (air T, humidity, wind) and physical and chemical oceanographic data (seawater T, salinity, currents, waves, dissolved oxygen).

Figure 2(c) presents the image of the Vida buoy and its geographical position approximately 2 nautical miles away from Piran at the Adriatic coast in Slovenia (coordinates 45° 32.925′ N, 13° 33.042′ E) (Figures 2[d] and [e]). The framework carrying the racks with samples was lowered from the boat and positioned at a depth of 20 m (video given in Supplemental Video SV1). The frame with racks was secured at the sea bottom and tied to the buoy (Figure 2[f]). Therefore, the samples were exposed to the natural sea movements at this depth but firmly attached to the frame.

The test duration was 8 months, from July 25, 2017 to March 13, 2018. Samples were taken out on August 25, 2017 (after 1 month), October 26, 2017 (after 3 months), and March 13, 2018 (after 8 months).

† Trade name.

FIGURE 2. *(a) Individual sample, (b) frame with racks with samples, (c) removal of the racks with samples from the seawater near the buoy, (d, e) maps of the immersion site (coordinates 45° 32.925; N, 13° 33.042' E), and (f) positioning of the racks with samples at a depth of 20 m.*

Data on sea temperature at the sea bottom and the surface, salinity at the surface, and concentration of oxygen at the sea bottom were provided by MBS based on the data collected at the Vida buoy (Figure S1). From July 2017 to March 2018 (32 weeks), the surface temperature of seawater gradually changed from summer to winter conditions decreasing from ca. 26°C to 27°C to 8°C. The bottom temperature reached the maximum of ca. 23°C in October 2017 and then decreased in the winter, when bottom and surface temperatures were equal. Salinity slightly varied depending on the season and increased from summer to winter from 35 to 38 per mille. These variations are related to the freshening by rivers.[33] The oxygen concentration at the sea bottom varied between 320 µmol/L and 280 µmol/L, reaching a minimum in October 2017.

2.2.3 | Treatment of the Immersed Samples

After removal from the sea, racks were photographed using a high-resolution digital camera before demounting the samples (Figure S2[a]). Once the rack was safely positioned in the boat, samples were removed and transferred to vials (Figures S2[b] and [c]). Two samples out of triplicate were transferred to polyethene vials (volume 150 mL) filled with physiological Ringer solution (B. Braun, Melsungen, Germany). The composition of the Ringer solution is 8.6 g/L NaCl, 0.3 g/L KCl, and 0.33 g/L $CaCl_2 \times 2H_2O$. The third sample out of triplicate was transferred to a polyethene vial (volume 150 mL) filled with seawater.

Once samples were delivered to the laboratory (Figures S2[d] through [f]), they were processed further according to the scheme presented in Figure 1. Two vials filled with Ringer solution were sonicated in the same solution (vortexed 30 s, sonicated at 40 kHz for 10 min). The purpose of sonication was to remove the biofilm (biofouling) and microorganisms attached to the samples' surface during immersion. Samples were photographed using a high-resolution digital camera before and after sonication to document biofilm removal. After sonication, samples were taken out of sonicates, air-dried, and stored in new polyethene vials for further measurements, i.e., electrochemical measurements, XPS, GDOES, and SEM/EDS analyses. Electrochemical measurements were performed on sonicated samples immersed for 1, 3, and 8 months, XPS and GDOES analyses after 1 month, and SEM analysis after immersion for 1 and 8 months.

The biofilm-coated samples placed in a vial filled with seawater were processed further in the laboratory to prepare the surface for SEM analysis. Samples covered with biofilm and attached microorganisms require chemical fixation to preserve and stabilize their structure.[34] The fixation process was performed by immersion for 5 min in a 25 vol% solution of glutaraldehyde (25 vol%, Sigma). This step was followed by dehydration of the fixed biological matter using an organic

solvent, i.e., ethanol (EtOH), which replaces water in the cells and preserves their structure. Immersion in progressively increasing EtOH concentration was applied: 5 min in 70% EtOH, 5 min in 95% EtOH, and 5 min in absolute EtOH (Carlo Erba, Milan, Italy). Samples were then air-dried and stored in new polyethene vials until the SEM analyses. SEM analyses were performed on biofilm-coated samples immersed for 1 and 8 months.

2.3 | Characterization Methods

A scanning electron microscope (SEM, JEOL JSM 5800†) and a field-emission scanning electron microscope (FE-SEM, JEOL JSM 7600F†, Tokyo, Japan) were used to analyze the morphology of the following samples: (i) nonimmersed samples, (ii) samples covered with biofilm, and (iii) sonicated samples after removal of the biofilm. Before SEM analysis, a thin carbon layer was deposited on the samples' surface. The imaging was performed using a secondary electron detector (SE mode) at 10 kV (JSM 5800) and 0.5 kV (JSM 7600F).

Morphology and composition of nonimmersed and immersed, sonicated samples were analyzed by a FIB-SEM (FEI Helios NanoLab 650† Dual-beam). SEM imaging was performed using CBS (circular backscattered detector) and ICE (ion charged detector) modes at 15 kV beam voltage. The cross sections of selected regions on the samples were obtained after the deposition of a thin layer of platinum on the surface (the first layer, 0.2 µm thick, was deposited using an electron beam at 2 kV and 0.4 nA, the second layer, 1 µm thick, was deposited using Ga FIB beam at 30 kV and 0.24 nA), followed by cutting the coating using Ga FIB beam at 30 kV and 9.4 nA. The surface was polished with a Ga beam at 30 kV and 0.4 nA in the last step. Imaging along the cross section was performed by SEM using SE mode at 15 kV. The top surface and cross-section compositions were determined by EDS using an Oxford† Instruments AZtec system with an X-max SDD 50 mm^2 (silicon drift detector). The EDS analyses were performed at 15 kV, 5 kV, or 3 kV in a point analysis. The data were normalized to atomic percentages (at%). The amount of carbon was excluded from the quantitative analysis. EDS mapping was recorded at 15 kV.

The CASINO† program (version v.2.51, University of Sherbrooke, Canada), a single scattering Monte Carlo simulation of electron trajectory in solid, specifically designed for low energy beam interaction was used to generate many recorded signals (x-rays and backscattered electrons) in a SEM.

Table 2. *The Composition of Artificial Seawater (Burkholder formulation B), pH = 7.4.*

Compound	g (L)
$MgSO_4 \times 7H_2O$	6.805
$MgCl_2 \times 6H_2O$	5.01
$NaHCO_3$	0.192
KCl	0.664
NaCl	26.702
$CaCl_2 \times 6H_2O$	1.469
KBr	0.096
H_3BO_3	0.026
$SrCl_2 \times 6H_2O$	0.040

The surface characterization of elemental composition and chemical state of the elements was performed by XPS using Thermo Electron ESCALAB 250† spectrometer, with a monochromated Al Kα x-ray source (hν = 1,486.6 eV). The base pressure in the analytical chamber was maintained at 10^{-9} mbar. The spectrometer was calibrated using Au $4f_{7/2}$ at 84.1 eV. The take-off angle of analyzed photoelectrons was 90°. The analyzed area was a 500 µm diameter disk. Survey spectra were

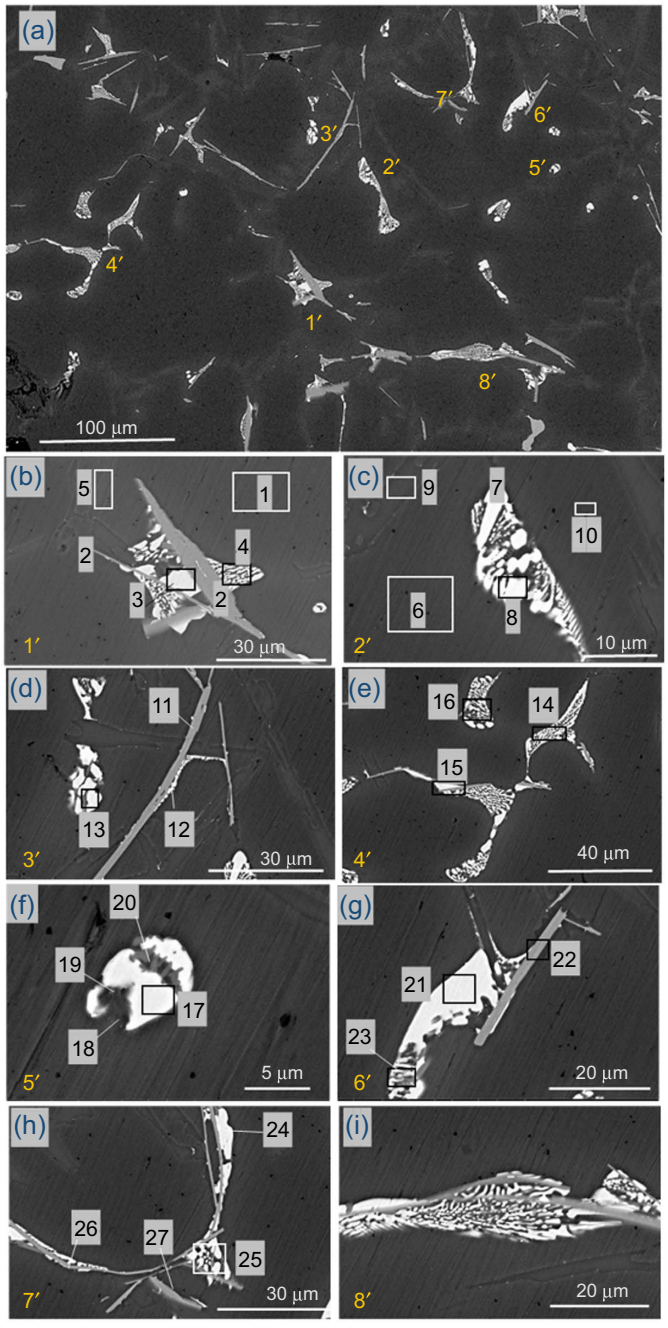

FIGURE 3. *SEM (CBS mode) images of the microstructure of Al-Si9-Cu3 with eight representative types of intermetallic particles numbered 1′ to 8′ in (a). IMPs are detailed in (b) through (i). EDS analysis was made on the numbered sites 1 to 27; the results are presented in Table 3. For the intermetallic particle presented in (i), the EDS mapping is presented in Figure 4. SEM and EDS analyses were made at 15 kV.*

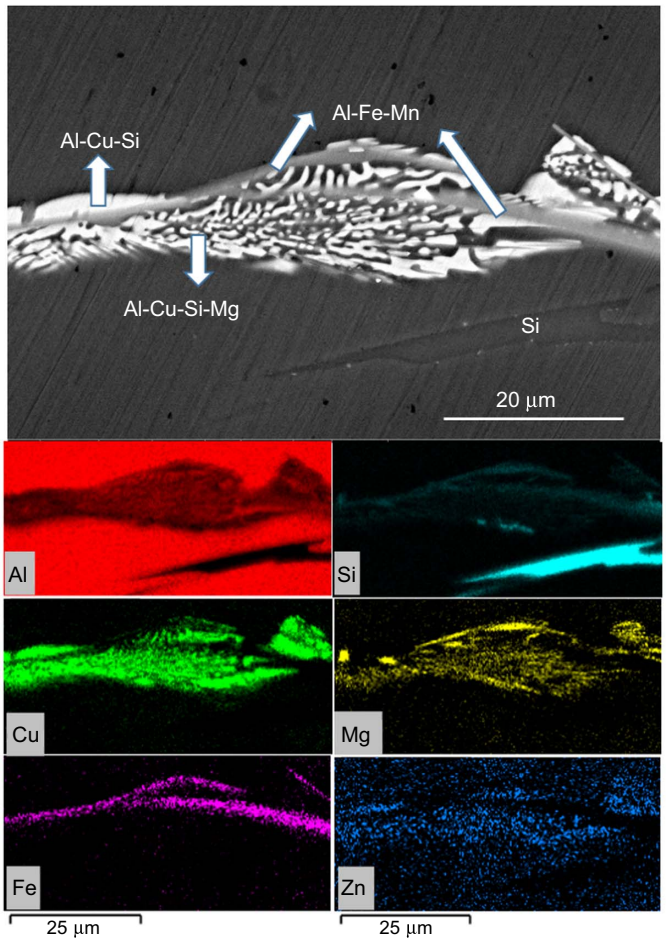

FIGURE 4. *SEM image (CBS) mode and elemental EDS mapping of the selected IMP of Al-Si9-Cu3 (SEM image in Figure 3[i]). SEM and EDS analyses of elemental mapping were made at 15 kV.*

recorded with a pass energy of 100 eV at a step size of 1 eV and high-resolution spectra with a pass energy of 20 eV at 0.1 eV. Curve fitting of the spectra was performed with the Thermo Electron† software Avantage using iterative Shirley-type background subtraction. All spectra were aligned with the C1s peak for carbon involved in C–C and C–H bonds, located at 285 eV. For some samples, a strong charging effect was observed. The position of all XPS peaks was aligned with the position of the reference C1s peak. The values of the photoionization cross sections (σ_X) at 1,486.6 eV were taken from Scofield,[35] the inelastic mean free paths (λ_X^Y) were calculated by the TPP2M formula.[36] The compositions presented in the tables are deduced from high-energy resolution spectra.

The additional elemental indepth profiling was performed using GDOES (GD-PROFILER2†, HORIBA Scientific), identifying the elemental composition rapidly through the coating. Operating conditions were: anode diameter 4 mm, argon pressure 850 Pa, and applied radiofrequency (RF) power 35 W.

Electrochemical measurements were performed using a three-electrode flat cell (KO235 Flat Cell Kit†, Ametek, Berwyn, PA, USA) with a volume of 250 mL. Specimen embedded in a Teflon holder leaving an area of 1 cm^2 exposed to solution served as the working electrode. A silver/silver chloride (Ag/AgCl, 0.205 V_{SHE} [standard hydrogen electrode]) served as a reference electrode, and a platinum mesh as a counter-electrode. Potentials in the text refer to the Ag/AgCl scale. Electrochemical measurements were performed at room temperature in artificial seawater (Burkholder formulation B, pH 7.4). The composition of artificial seawater was given in Table 2.[37] The chemicals were supplied by Sigma-Aldrich ($MgSO_4 \times 7H_2O$, $NaHCO_3$, KCl), Acros Organics ($MgCl_3 \times 6H_2O$, $CaCl_2 \times 6H_2O$, KBr, $SrCl_2 \times 6H_2O$), Fisher Chemicals (NaCl), and Riedel-de-Haën (H_3BO_3). Measurements were conducted using an Autolab potentiostat/galvanostat Model 302N† (Utrecht, The Netherlands).

Electrochemical measurements were performed on non-immersed samples and samples immersed in the Adriatic

Table 3. *The Composition of the Surface of Al-Si9-Cu3 Measured by EDS at Different Sites at the Matrix and Intermetallic Particles (SEM Images in Figure 3)*[(A)]

Description	Spectra	Composition (at%)								
		Al	O	Si	Cu	Zn	Fe	Mn	Mg	C
Matrix, dark gray	1, 6, 10	95.2	2.0	1.2	1.1	0.5	–	–	–	–
Si(Al), black	5, 9	3.6	–	96.4	–	–	–	–	–	–
Al-Si-Fe(Mn), bright gray, longitudinal	2, 11, 22, 26	67.4	–	18.4	–	–	12.5	1.7	–	–
Al-Cu(Si,C), bright, solid	15, 17	59.9	1.6	1.6	24.7	–	0.4	–	0.2	11.6
Al-Cu(Si), bright, solid	3, 7, 8, 13, 21, 24	65.8	1.0	1.8	31.1	–	0.3	–	–	–
Al-Cu(Si,Mg), bright, patterned	4, 12, 14, 16, 23, 25	71.2	1.9	6.1	13.9	–	–	–	6.9	–
Al-Si-Cu, black, solid	18, 19	45.3	0.7	48.8	4.5	0.3	–	–	0.4	–
Al-Si-Mg-Cu, gray	20	48.5	1.6	23.3	9.9	–	–	–	16.7	–
Si-Al(Fe), gray, longitudinal	27	37.9	–	54.9	–	–	7.2	–	–	–

[(A)] Nine characteristic compositions were recognized (first column). For each of them, the representative elemental composition is given. The sites at which the particular compositions were determined are noted in the second column. EDS analysis was made at 15 kV.

Sea for 1, 3, and 8 months. On each sample, measurements were performed on three sites after biofilm removal by sonication. After 8 months of immersion, it was difficult to remove the biofouling by sonication and, consequently, to find several spots at the surface to perform more repetitions. Therefore, the measurements are taken with caution and are presented with different symbols than those after 1 and 3 months of immersion.

Each sample was subject to four successive measurements from least destructive to more destructive methods, including open-circuit stabilization, linear polarization resistance (LPR) measurements, electrochemical impedance spectra, and potentiodynamic polarization curves. Before switching to the following electrochemical technique, the system was allowed to rest for 5 s. (i) The sample was first allowed to rest at open-circuit potential for approximately 1 h to reach a stable, quasi steady-state open-circuit potential (E_{oc}) at the end of the rest period. (ii) LPR curves were then recorded in the range from −10 mV to 10 mV vs. E_{oc} using a 0.1 mV/s potential scan rate. Polarization resistance (R_p) was determined as the slope of the fitted potential (E) vs. current density (j) curve using Nova 2.1† software. (iii) Electrochemical impedance spectra (EIS) were recorded at E_{oc} in the frequency (f) range from 100 kHz to 0.01 Hz using an AC potential amplitude of 10 mV (rms). (iv) Potentiodynamic polarization curve was recorded in the potential region starting from −250 mV vs. E_{oc} in the anodic direction until the current density reached 0.001 A/cm^2. Corrosion current density (j_{corr}) and corrosion potential (E_{corr}) were determined using Nova 2.1 software using extrapolation of the linear portion of polarization curves, i.e., Tafel extrapolation, based on the mixed potential theory.[38] j_{corr} was determined as the intersection of the anodic and cathodic Tafel slopes at E_{corr}. When it was impossible to assure a sufficient range of linearity of Tafel curves (up to 120 mV), especially in the anodic range, j_{corr} was determined as the intersection of the linear portion of the cathodic curve and the straight line passing through E_{corr}.

Quantitative electrochemical parameters are presented in tables as mean values±standard deviations. In graphs, representative measurements (at least two similar repetitions) were chosen to be presented.

RESULTS AND DISCUSSION

3.1 | Scanning Electron Microscopy/Energy Dispersive X-Ray Spectroscopy of Nonimmersed Substrates

3.1.1 | Al-Si9-Cu3 Alloy

The composition of the Al-Si9-Cu3 alloy is given in Table 1. The α-Al matrix contains eutectic Si grain boundaries and intermetallic particles (IMPs). The typical microstructure of Al-Si9-Cu3 is presented in the SEM image (CBS mode, Figure 3[a]). Eight types of particles were chosen to be analyzed by EDS (seven particles by point analysis (Figures 3[b] through [h]) and one by EDS mapping) (Figures 3 and 4). Table 3 depicts the types of particles sorted out according to their composition. α-Al matrix is composed mainly of Al, with a small amount of carbon and oxygen. Eutectic grains are composed mainly of silicon and appear as gray dendrite-like grains within α-Al matrix. Al-Si-Fe(Mn) particles appear bright gray in the CBS image and have a longitudinal shape (Chinese scripts).[39] Al-Cu particles (Cu-rich θ phase) appear bright. Some of those IMPs contain a higher content of carbon. Al-Cu-Si-Mg particles (Q phase) are also gray but patterned and contain more Si than θ phase. There are also Si-rich Al-Si-Cu(Mg) particles that appear black in the CBS image and Al-Si-Mg-Cu particles that appear gray and close to Al-Cu particles.

EDS mapping of one of the IMP sites is presented in Figure 4. Several typical particles are recognized: Al-Fe-Mn longitudinal particle, Al-Cu-Si particle located along with the Fe, Mn-containing particle, patterned Al-Cu-Si-Mg bright area, and Si-rich dark grains.

3.1.2 | Al-Si7-Mg0.3 alloy

The composition of Al-Si7-Mg0.3 is given in Table 1. Compared to Al-Si9-Cu3 alloys, Al-Si7-Mg0.3 contains less Si, Mg, Fe, Mn, and Zn, and significantly less Cu; overall, it contains a smaller amount of alloying elements and thus more Al.

The typical microstructure of Al-Si7-Mg0.3 is presented in the SEM image (CBS mode, Figure 5[a]). The α-Al matrix

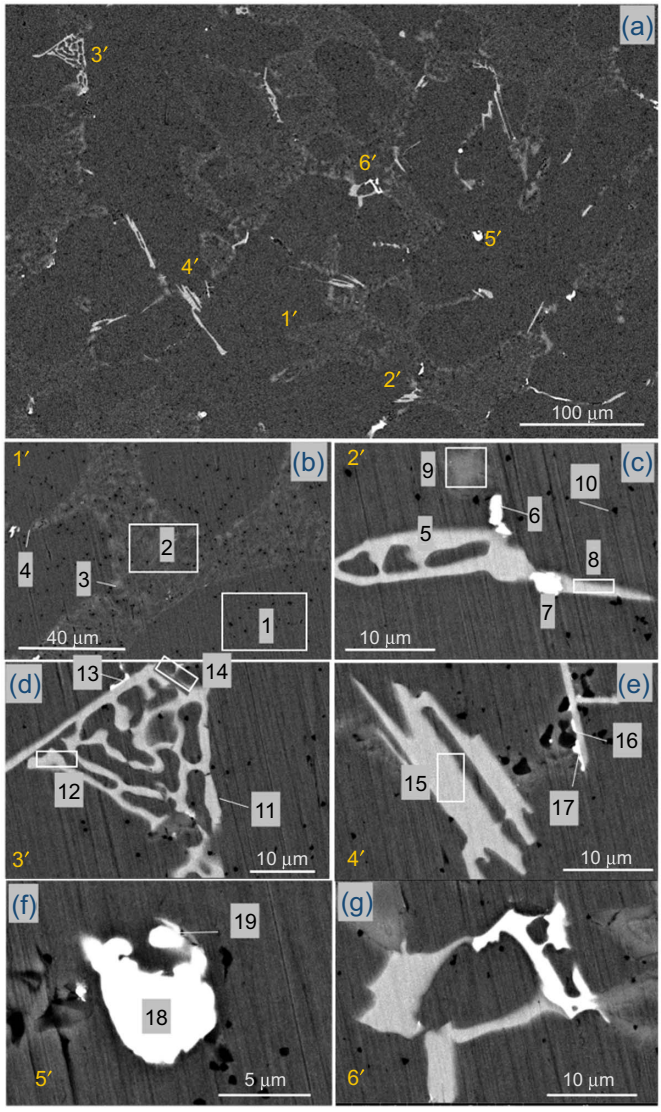

FIGURE 5. *(a) SEM (CBS mode) images of the microstructure of Al-Si7-Mg0.3 with six representative types of IMPs numbered 1′ to 6′. IMPS are detailed in (b) through (g). EDS analysis was made on the numbered sites 1 to 19; the results are presented in Table 4. For the intermetallic particle presented in (g), the EDS mapping is presented in Figure 6. SEM and EDS analyses were made at 15 kV.*

contains larger eutectic areas and a smaller number of IMPs, thus showing a different microstructure from the Al-Si9-Cu3 alloy where eutectic Si grains are spread on the smaller area, and different IMPs are present (Figure 3[a]). Six types of particles were chosen to be analyzed by EDS point analysis (Figures 5[b] through [g]), and for one type, the EDS mapping was made (Figure 6). Table 4 depicts the types of particles sorted out according to their composition. As for the Cu-containing alloy, α-Al matrix is composed mainly of Al, with a small amount of silicon and oxygen. Eutectic grains are Si-rich and appear gray dendrite-like grains within the α-Al matrix. Al-Si-Mn(Mg) particles appear bright gray in the CBS mode (Figures 5[b] through [g]). Some particles contain Mg or Fe, and others do not. Some are rich in carbon. The second main type of IMPs is Al-Si-Fe-Mn particles. The content of Fe is about several times greater than in Al-Si-Mn-Mg IMPs. Some contain more Mn than others, and some may be rich in carbon.[40] These particles are bright gray and appear larger than Al-Si-Mn (Mg) IMPs.

EDS mapping of one of the IMP is presented in Figure 6. Several typical particles are recognized: Al-Si-Fe-Mn particle, so-called Chinese scripts, Al-Si-Mg(Fe,Mn) particles, and Si-rich gray grains.

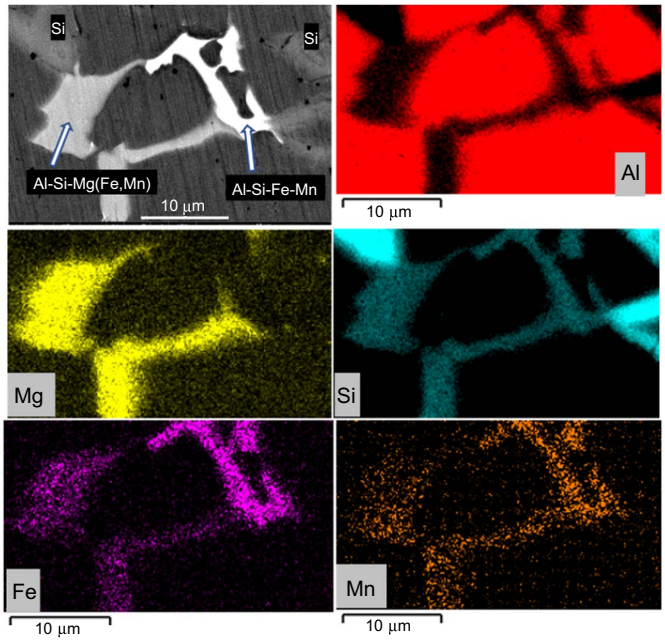

FIGURE 6. *SEM image (CBS mode) and elemental EDS mapping of the selected intermetallic particle of Al-Si7-Mg0.3 (SEM image in Figure 5[g]). SEM and EDS elemental mapping analyses were made at 15 kV.*

3.2 | Images of Samples Before and After Immersion in Seawater

Individual samples after immersion for 1, 3, and 8 months are presented in Figure 7. The progressive coverage of samples with biofouling and attached microorganisms is evident during prolonged immersion. Samples were imaged before and after sonication. The amount of biofouling increased with increasing immersion time; after 1 month, the surface was covered mainly by algae, whereas larger organisms were present after 3 months, especially after 8 months. Overall, it seems that the amount of biofouling is lesser on Al-Si7-Mg0.3 than on Al-Si9-Cu3, at least up to 3 months of immersion. The sonication of the samples immersed for 1 month removed the attached algae biofouling and even larger microorganisms. However, the sonication step could not remove all of the larger microorganisms after 3 months and especially after 8 months of immersion, and those remained firmly attached to the surface. A detailed description of the sample analysis is given in the *Experimental Procedures* section.

Copper acts like biocide when added to paints for marine vessels.[41] We did not observe the effect that Cu present in the alloy would mitigate the amount of biofoul, probably because it acted as a cathode in IMP. A more focused study would be required to address the effect of Cu in the alloy on the amount of biofouling.

Table 4. *The Composition of the Surface of Al-Si7-Mg0.3 Measured by EDS at Different Sites at the Matrix and Intermetallic Particles (SEM Images in Figure 5)*[(A)]

Description	Spectra	Composition (at%)						
		Al	O	Si	Fe	Mn	Mg	C
Matrix, dark gray	1	96.1	2.5	1.4	–	–	–	–
Si-Al(C), eutectic, patterned	2, 3, 9, 14	16.6	0.6	69.7	–	0.2	–	12.9
Al-Si-Mg(Fe), gray	5, 8, 11, 12, 15	58.0	–	23.3	3.5	1.0	14.2	–
Al-Si-Mn-Mg, bright	7, 16	62.8	–	20.6	1.2	7.3	8.1	–
Al-Si-Mg(C), bright	17	62.3	1.1	13.0	1.4	1.0	9.0	12.2
Al-Si-Fe-Mn, bright	4, 18	71.8	–	11.2	10.2	6.8	–	–
Al-Si-Fe-Mn(Mg), bright	13, 19	73.2	3.2	9.7	6.6	5.2	2.1	–
Al-Si(Fe, Mn, C), bright	6	73.7	–	6.0	4.5	3.2	0.3	12.2
C-Al, dark	10	31.3	0.8	0.3	–	–	0.1	67.5

[(A)] Nine characteristic compositions were recognized (first column). For each of them, the representative elemental composition is given. The sites at which the particular compositions were determined are noted in the second column. EDS analysis was made at 15 kV.

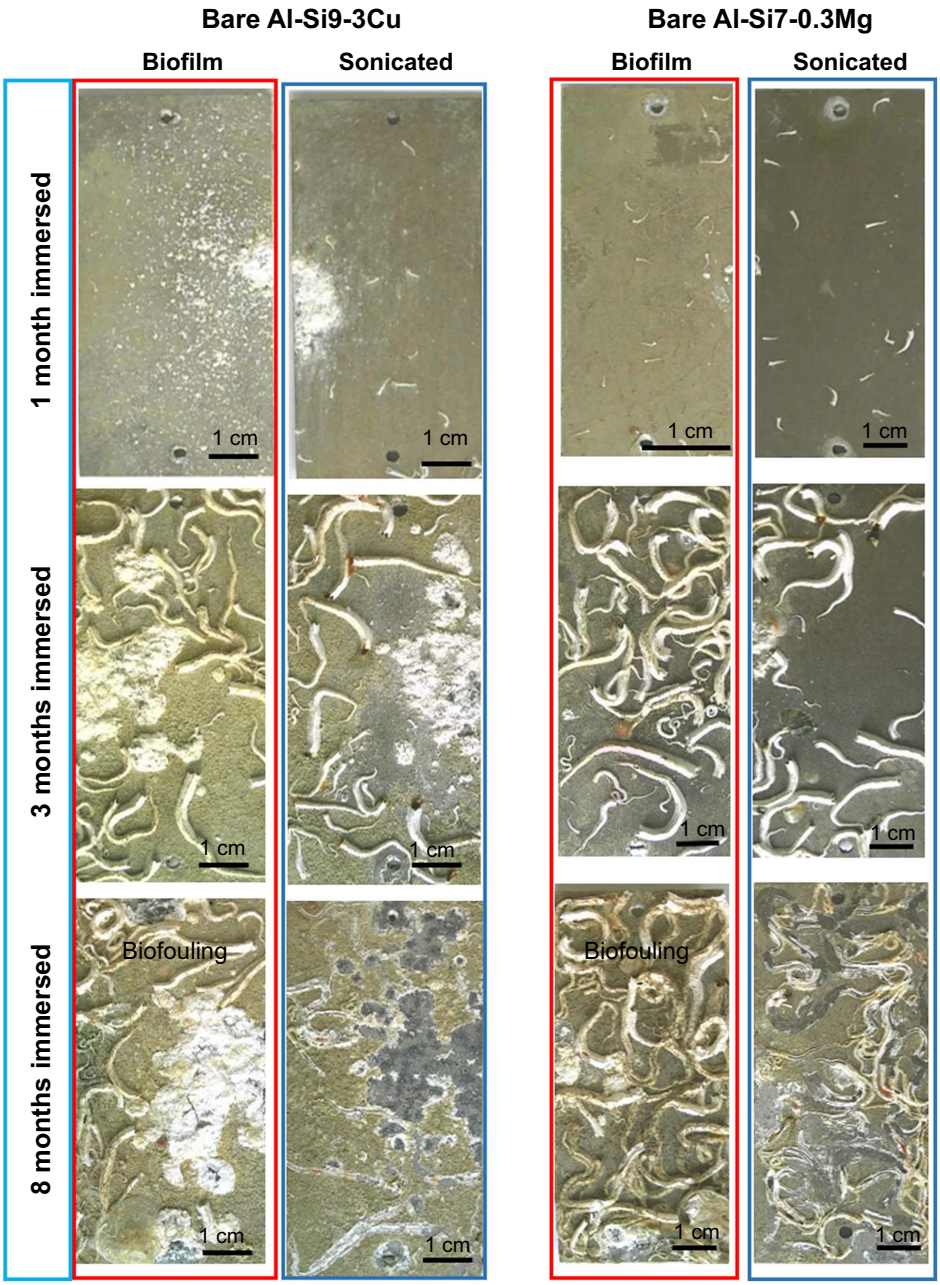

FIGURE 7. *Photos of Al-Si9-Cu3 and Al-Si7-Mg0.3 samples after 1, 3, and 8 months of immersion in the Adriatic Sea covered with biofilm and after partial removal of the biofilm (biofouling) by sonication.*

3.3 | Scanning Electron Microscopy/Energy Dispersive X-Ray Spectroscopy Before and After Immersion in Seawater

3.3.1 | Al-Si9-Cu3 Alloy

SEM images of Al-Si9-Cu3 bare samples imaged after 1 and 8 months of immersion in the Adriatic Sea are presented in Figure 8 (5,000×) and Figure S3 (1,000×) for both biofouling-covered and sonicated conditions. Before immersion, the surface of the bare sample shows a relatively rough surface with grinding marks and individual defects (Figure S3[a]). After 1 month of immersion, the Al-Si9-Cu3 sample was covered by a thick layer of biofouling (mainly diatoms) (Figures 8[a] and S3). SEM images after 8 months show the increased amount of biofouling and more than 20 μm large diatoms (Figures 8[c] and S3d).

Once the majority of the biofouling layer was removed by sonication, the formation of a several micrometers thick surface layer formed in the immersion course was evident (Figures 8[b], [d], S3[c], and [d]). Detailed SEM/EDS analysis of the surface layer is presented in Figure 9 and Table 5. The cracks were observed throughout the layer surface. It is difficult to state whether the cracks were formed during the formation of this layer in seawater or during SEM analysis due to the dehydration of the surface in the vacuum chamber. The surface layer was formed over the matrix and IMPs (Figure 9). A gray area represents the layer formed over α-Al matrix, whereas brighter areas denote the layer formed above IMPs-containing Fe and Cu.

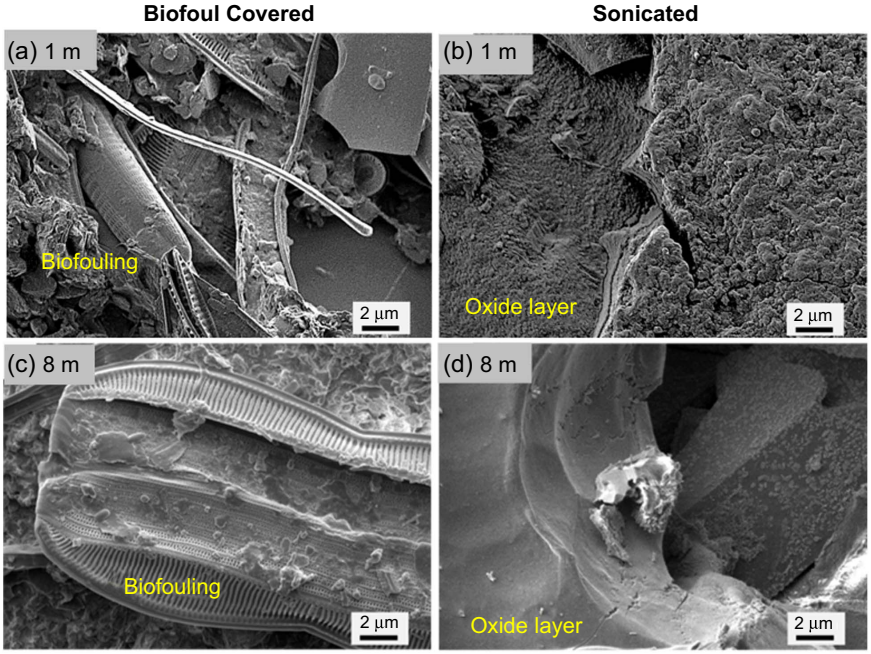

FIGURE 8. *SEM images (SE mode) of the Al-Si9-Cu3 samples after immersion for (a, b) 1 month and (c, d) 8 months in the Adriatic Sea: (a, c) biofouling covered and (b, d) after removal of biofilm by sonication. Magnification 5,000×. SEM images recorded for nonimmersed and immersed samples at a magnification of 1,000× are given in Figure S3. SEM analysis was made at 15 kV.*

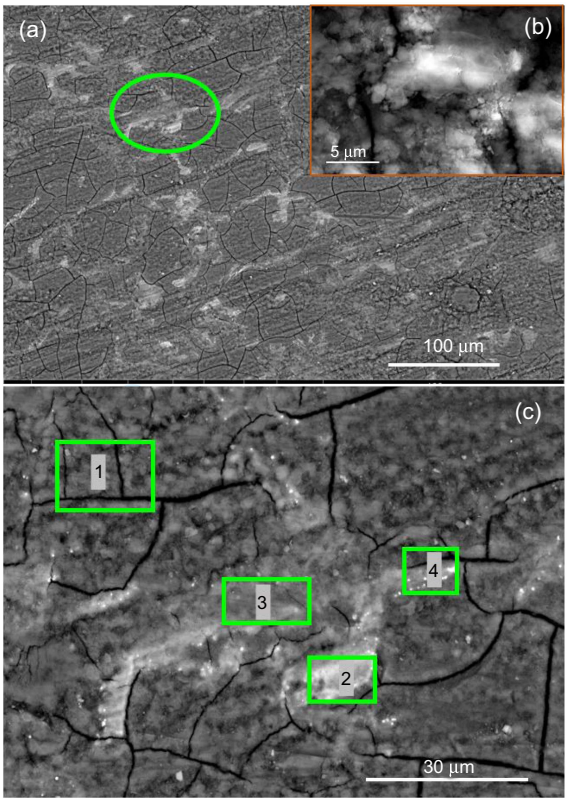

FIGURE 9. *SEM images (CBS mode) of the surface of the Al-Si9-Cu3 sample after immersion for 1 month in the Adriatic Sea and lower and higher magnifications. The site where EDS analysis was made is denoted by a green circle in (a) and enlarged in (c). Enlarged detail of the oxide layer is presented in (b). EDS results at sites 1 to 4 are presented in Table 5. The sample was sonicated before the analysis.*

The composition of the surface layer over α-Al matrix (spectrum 1) confirms the formation of Al-Mg-oxide (Table 5). The large oxygen concentration of over 50 at% reflects the oxide formation. Among cations, Al is most abundant (26 at%), followed by Mg (4.3 at%), and Si (1 at%). When the analysis was made at the sites above IMPs (spectra 2 to 4), elements originating from IMPs were also detected, namely Cu, Fe, and Mn. At those sites, the concentration of Mg was even larger than on the matrix and reached 12.4 at%. The voltage was decreased from 15 kV to 3 kV to exclude the effect of the signals originating from the alloy bulk (spectra 5 and 6). By doing that, the analysis depth decreased from 3.5 µm (15 kV) to 0.8 µm (5 kV) and 0.35 µm (3 kV), thus preventing the elements from the bulk alloy (Cu, Fe, Mn) from being detected. A detailed explanation of the analysis depth calculation is given in Figure S4. Instead, only O, Al, Si, and Mg were identified using a 5 kV beam, and only O, Al, and Mg when using 3 kV. Thus, the surface layer consists mainly of Al-Mg oxide/hydroxide and contains some Si. The concentration of Mg in the surface layer is unexpectedly high, given that only 0.15 wt% to 0.55 wt% Mg (0.17 at% to 0.64 at%) is present in the bulk alloy (Table 1). Therefore, Mg concentration in the surface layer (4.3 at% to 12.4 at%, Table 5) is up to ten-fold concentration in the bulk alloy.

The SEM image of the cross section is presented in Figure 10, together with EDS elemental mapping images. The oxide layer was visible at the top, with a large concentration of O, Al, and Mg. Below the surface oxide layer, IMPs with Al-Si-Fe-Mn and Al-Si-Cu-Zn particles were present. Between IMP and the top oxide layer, there is an Al-Mg-Zn matrix.

Judging roughly from the cross section, the thickness of the top oxide layer is in the micrometer range. FIB-SEM image taken at the beginning of cutting through the coating is presented in Figure S5(a). An enlarged image of the yellow

Table 5. *The Composition Determined by EDS Point Analysis Made at the Different Sites on the Surface (Matrix and IMPs) of the Al-Si9-Cu3 Sample After Immersion for 1 month in the Adriatic Sea (SEM images in Figure 9)*[A]

Spectra	Composition (at%)								
	Al	O	Si	Cu	Zn	Fe	Mn	Mg	C (minor elements)
15 kV									
1	25.7	54.6	1.0	–	–	–	–	4.3	13.5 (0.9)
2	19.3	30.6	2.8	1.1	–	4.4	0.8	3.4	37 (0.5)
3	21.5	54.3	8.7	1.6	–	3.1	0.5	8.6	(1.4)
4	15.5	61.7	2.6	5.0	0.4	–	–	12.4	(2.3)
5 kV									
5	10.5	56.6	1.8	–	–	–	–	8.8	22.3
3 kV									
6	15.4	73.7	–	–	–	–	–	10.9	–

[A] EDS analysis was made using different voltages.

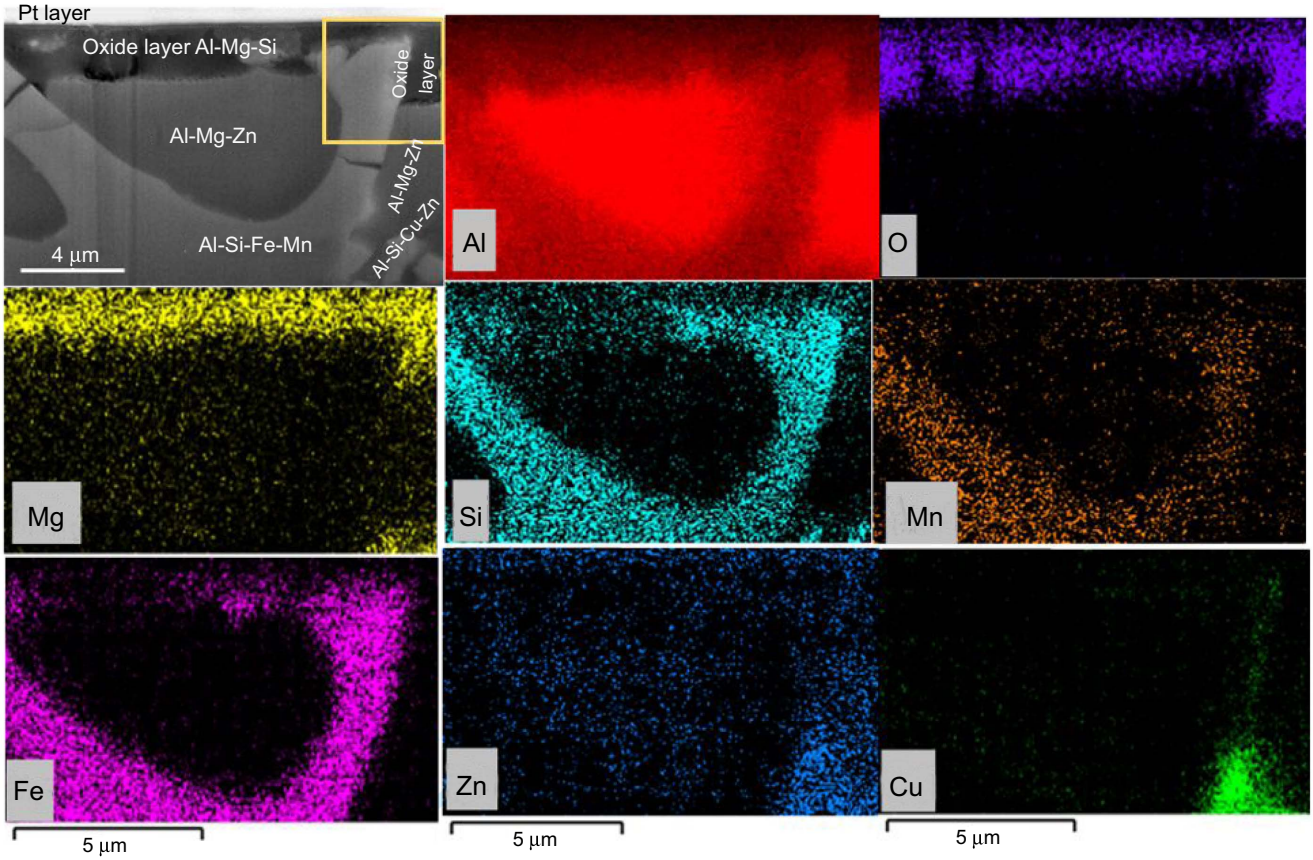

FIGURE 10. *SEM image (CBS mode) of the cross section and EDS elemental mapping of the selected site on the Al-Si9-Cu3 sample after immersion for 1 month in the Adriatic Sea. SEM image recorded at the top of this site (before making the cross section by FIB) and related EDS analysis is given in Figure 9(b). SEM and EDS analyses were made at 15 kV. The sample was sonicated before the analysis. The area denoted by the yellow square in the SEM image is enlarged in Figure 11(a).*

rectangular area in Figure 10(a) is given in Figure 11(a). The thickness of the top surface oxide layer grew to over 700 nm above IMPs. In the area between IMPs, the thickness of the oxide layer is even larger, almost 2 µm. IMPs protruded through this layer highly enriched in Mg (Table 5, spectra 5 and 6).

3.3.2 | Al-Si7-Mg0.3 Alloy

SEM images of Al-Si7-Mg0.3 bare samples imaged after 1 and 8 months of immersion in the Adriatic Sea are presented in Figure 12 (5,000×) and Figure S6 (1,000×) for both biofouling-covered and sonicated conditions. Before immersion, the surface

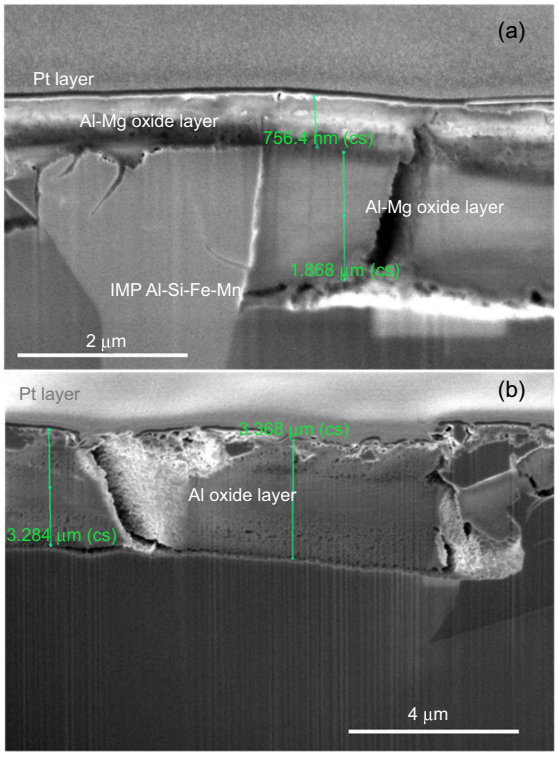

FIGURE 11. *FIB-SEM images (SE mode) of the cross section to show the thickness of the oxide layers formed on (a) Al-Si9-Cu3 and (b) Al-Si7-Mg0.3 samples after immersion for 1 month in the Adriatic Sea. SEM images were recorded at 2 kV. Related elemental EDS mappings are presented in Figure 10 for Al-Si9-Cu3 and Figure 14 for Al-Si7-Mg0.3. FIB-SEM images taken at the beginning of cutting through the coating are presented in Figure S5.*

of the bare sample shows a relatively rough surface with grinding marks and individual defects (Figure S6[a]). After 1 month of immersion (Figure 12[a]), the Al-Si7-Mg0.3 sample was covered by a biofouling layer, which seemed thinner than on Al-Si9-Cu3 (Figures 7 and 8[a]). The biofouling was removed by sonication (Figure 12[b]). SEM images after 8 months show the increased amount of biofouling and large diatoms, which were removed by sonication (Figures 12[c], [d], S6[d], and [e]).

The mode of formation of the surface layer during immersion of Al-Si7-Mg0.3 for 1 month reflects the microstructure of the underlying alloy (Figure 13[a]), as is evident by the comparison with the nonimmersed sample (Figure 5). Two regions with distinct morphological differences are formed: (i) the layer formed above the α-Al matrix is relatively homogeneous and dense (area 2', Figure 13[a]) and (ii) the layer formed above Si-rich eutectic grains is different and incorporates micrometer-long grains of different composition (area 1', Figure 13[a]). These regions can be correlated with the matrix (spectrum 1, site 1, Figure 5[a]) and eutectic, Si-rich areas (spectrum 2, site 1, Figure 5[a]). At high magnification, the differences between the two regions became clearer (Figure 13[c]).

These layers also differ in composition, as identified by point EDS analysis (Table 6). The layer formed on the α-Al matrix (spectrum 3, Figure 13[c]) was composed mainly of Al-oxide; it contains some Mg (ca. 1 at%) and Si (ca. 2 at%). In contrast, the Al-oxide layer formed in the eutectic region was rich in silicon (spectrum 1, Figure 13[c]), with incorporated Si-rich grains (spectrum 2). The latter contained a double concentration of Si (ca. 38 at%) compared to the surrounding layer (ca. 17 at%). The concentration of Mg remained around 1 at%. Similar ratios were obtained when the EDS analysis was made using 5 kV beam voltage, indicating that the Si signal originates from the surface layer and the alloy bulk (depth analysis was 3.7 µm at 15 kV

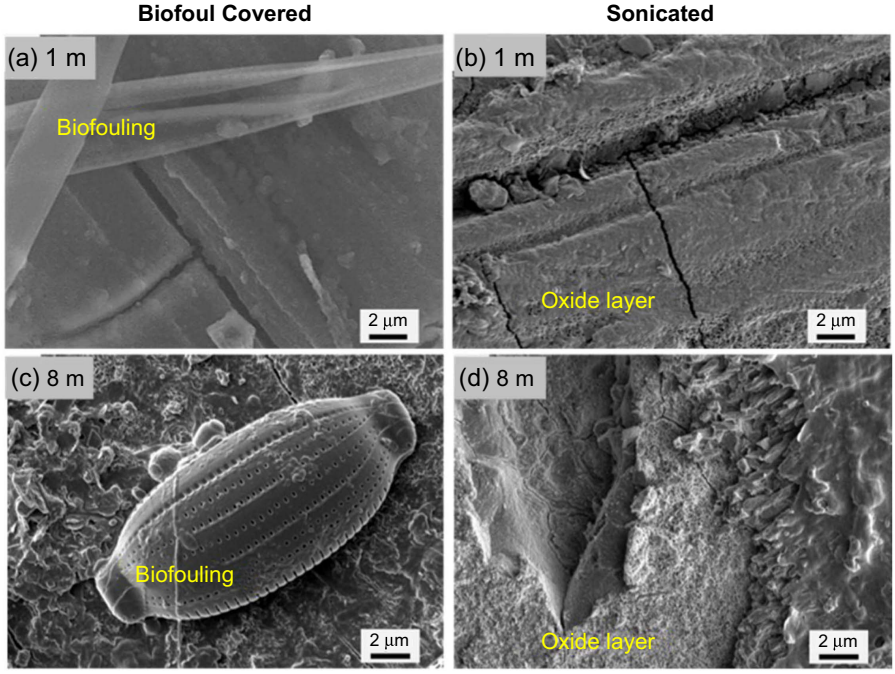

FIGURE 12. *SEM image (SE mode) of the Al-Si7-Mg0.3 samples after immersion for (a, b) 1 month and (c, d) 8 months in the Adriatic Sea: (a, c) biofouling covered and (b, d) after removal of biofilm by sonication. Magnification 5,000×. SEM images recorded for nonimmersed and immersed samples at a magnification of 1,000× are given in Figure S6. SEM and EDS analyses were made at 15 kV.*

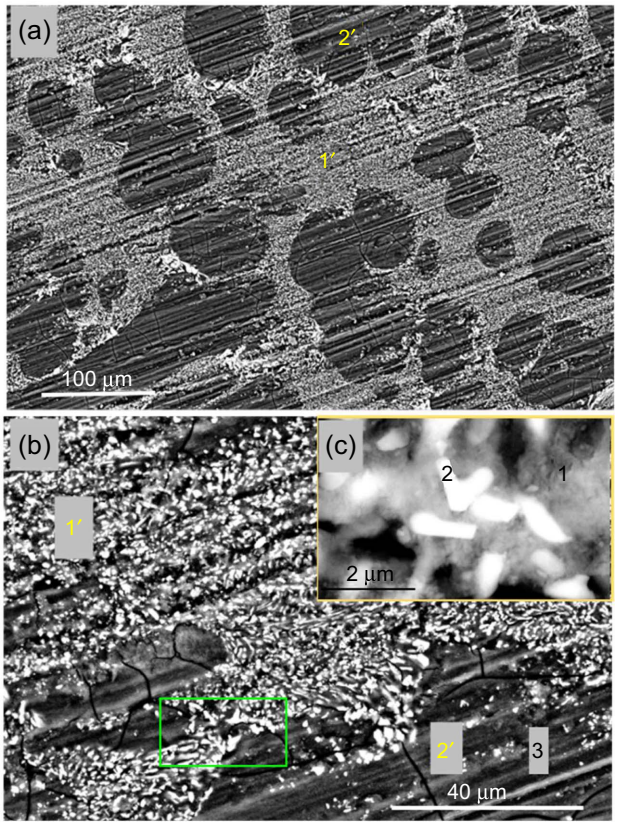

FIGURE 13. *SEM images (CBS mode) of the surface of the Al-Si7-Mg0.3 samples after immersion for 1 month in the Adriatic Sea. The sample was sonicated before the analysis. Two distinct areas are recognized: (1′) covered with a thick oxide layer containing Si-rich particles and (2′) covered with a thin oxide layer. Different magnifications are used in (a) and (b). The EDS analysis was made at the numerated sites 1 and 2 in (c), and 3 (b); the results are presented in Table 6. The green rectangle denotes the spot where the FIB cross section was made (Figure 14). SEM and EDS analyses were made at 15 kV. The sample was sonicated before the analysis.*

and 0.9 µm at 5 kV, as explained in Figure S7). Therefore, the layer formed on the α-Al matrix was mainly Al-oxide with minor amounts of Mg and Si, whereas the layer formed in the eutectic region was Al-oxide mixed with Si. Compared to the oxide formed during immersion on the Al-Si9-Cu3 alloy, this layer contained only a small amount of Mg, around 1 at%.

Based on the point analysis, it was difficult to establish whether Si-rich grains in the Al-oxide are Si in the oxidized state. However, cross-section analysis revealed that these grains are composed almost entirely of silicon (Figure 14). FIB-SEM image taken at the beginning of cutting through the coating is presented in Figure S5(b). The oxide layer on the top contained mainly Al-oxide, with a thickness exceeding 3 µm (Figure 11[b]). EDS mapping confirmed that the grains in this oxide layer are composed almost exclusively of silicon and contain a much lower oxygen concentration than the top oxide layer. Silicon and iron IMPs are cathodic relative to the aluminum matrix.[40] The shape of Si-rich grains is either longitudinal, several micrometers long and up to 500 nm wide, or irregular quadrilateral shape. Under the surface oxide, IMP composed of Fe-Mg was present within the alloy matrix.

3.4 | X-Ray Photoelectron Spectroscopy and Glow Discharge Optical Emission Spectroscopy Before and After Immersion in Seawater

3.4.1 | Al-Si9-Cu3 Alloy

The composition of the oxide at the surface of the nonimmersed and immersed Al-Si9-Cu3 sample is presented in Table 7. The composition was calculated with and without oxygen content to look closer at the cationic fraction (ratio of metal species in the oxide layer). High-resolution spectra of the main elements Al, O, Si, and Mg are presented in Figure 15; survey and high-resolution spectra of minor elements are presented in Figures S8 and S9, respectively.

The surface of the nonimmersed sample is covered by a naturally formed oxide layer containing mainly Al oxide (Al/Si = 10.5 and Al/Mg = 26.7). Two peaks appeared in the Al2p spectrum, at 75.7 eV and 72.8 eV reflecting the presence of Al(III) oxide/hydroxide on top of Al metal (Figure 15). An oxide layer thickness of 2.8 nm is calculated from the ratio of Al metal and Al (III) peaks. The O1s peak is centered at 533.1 eV. Si is the most intense among alloying elements, showing Si2p peaks at 99.4 eV and 103.6 eV, respectively, aligned with the presence of Si metal and Si(IV) oxide.[42] Mg2p peak is located at 51.8 eV, which may be related to the presence of Mg(II) in MgO, $Mg(OH)_2$, and/or Mg-Al-Si-oxides.[42] Cu2p and Zn2p peaks are much less intense (Figure S9). In the Cu2p core level, the peak at 933.8 eV can be attributed to Cu metal in IMPs or Cu(I).[43] The Zn peak at 1,023.7 eV can be attributed to metallic or oxidized Zn.[43]

After immersion, a single peak at 75.7 eV was present in the Al2p spectrum; similarly, a single peak at 103.6 eV was

Table 6. *The Composition Determined by EDS Point Analysis Made at the Different Sites on the Surface (Matrix and IMPs) of the Al-Si7-Mg0.3 Sample After Immersion for 1 month in the Adriatic Sea (SEM Images in Figure 13)*[(A)]

Spectra	Composition (at%)							
	Al	O	Si	Cu	Fe	Mn	Mg	C (minor elements)
15 kV								
1	33.6	35.9	16.7	–	–	–	0.4	12.1 (1.3)
2	26.2	34.4	37.8	–	–	–	1.4	(1.3)
3	40.5	54.9	1.7	–	–	–	0.9	(1.9)
5 kV								
1	30.5	58.4	7.4	–	–	–	0.5	(1.3)
2	30.4	52.6	14.1	–	–	–	1.5	(2.4)

[(A)] EDS analysis was made using different voltages.

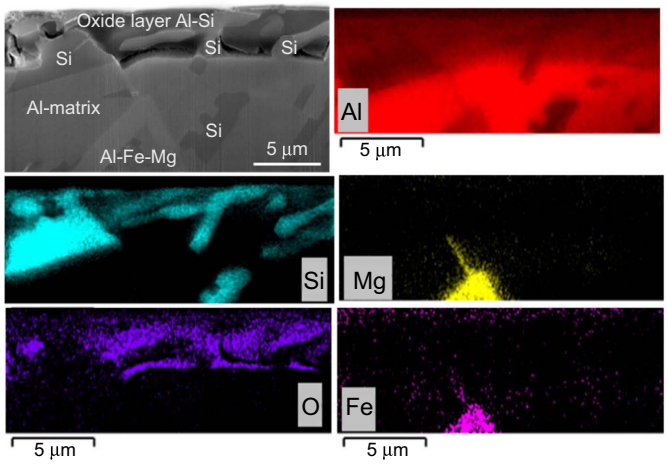

FIGURE 14. *FIB-SEM image (CBS mode) of the cross section and EDS elemental mapping of the selected site on the Al-Si7-Mg0.3 sample after immersion for 1 month in the Adriatic Sea. SEM image recorded at a lower magnification at the top of this site (before making the cross section by FIB) is given in Figure 13(b) (green rectangle). SEM and EDS analyses were made at 15 kV. The sample was sonicated before the analysis.*

present in Si2p spectrum (Figure 15). The peaks related to Al and Si metals were no longer visible due to the coverage of the surface with the oxide layer formed upon immersion in seawater. The Mg2p peak was strongly increased, reflecting Mg oxide or mixed Mg-Al oxide formation. The related ratios are Al/Si = 2.4 and Al/Mg = 2, showing a strong reduction compared to the nonimmersed sample (Table 7). Zn and Cu are either dissolved or buried below the surface layer, so these elements were not detected. Nitrogen and chlorine peaks appeared (Figure S9). Nitrogen N1s peak at 400 eV is presumably related to the organic matter of biofouling remaining after sonication. C1s peak is broader than a nonimmersed sample, indicating additional carbon species, presumably related to residual biological matter.

To summarize, after 1 month of immersion, the Al signal is much less intense, but Si and Mg are enriched at the surface compared to the spectra before immersion (Table 7, Figure 15). Seven-fold enrichment of the oxide layer in Mg and almost three-fold enrichment in Si was observed. The oxygen signal remained high. The intensity of Cl2p is very small, indicating that the incorporation of chloride from seawater in the solid surface layer remaining after sonication is negligible. Therefore, XPS results confirm the SEM/EDS results (Figures 10 and 11[a]) concerning the enrichment of the oxide layer in Si and especially Mg.

GDOES was performed on samples before and after immersion in seawater. A large number of elements were monitored during the chemical profiling (Al, Mg, Cu, Si, O, H, C, N, S, P, K, Zr, Cl, Ca, and Na), but for better clarity, only the elements showing major modifications are presented. Figure 16(a) shows the evolution of the major elements of the alloy (Al, Cu, and Si) and the oxygen used as a marker for the oxides and/or hydroxide species before and after immersion. Before immersion, the rapid increase followed by stabilization of Al, Cu, and Si signals indicates that the bulk alloy has been reached. This information is confirmed by the fast decrease of the O signal probing the native oxide covering the alloy.

After immersion in seawater, the GDOES profile is strongly modified. Particularly, O is present in the early stages of the profile (0 s to 40 s). Combined with the decrease or absence of characteristic major elements of the alloy (Al, Cu, Si), it can be concluded that a thin oxide is present at the surface of the alloy. During this time, the Al signal presents a plateau (not visible for Cu and Si), suggesting the formation of mainly aluminum oxide. The stabilization of all signals (after a sputtering time of 60 s) at values similar to those obtained before immersion indicates that the bulk alloy has been reached.

Figure 16(b) shows recorded signals of Ca, Mg, Na, O, S, and Cl during the GDOES profiling of the immersed alloy. Two distinct domains can be observed during this chemical profiling with the presence of an oxide layer in the first seconds of sputtering (0 s to 25 s) followed by an interfacial domain enriched in Ca, Na, and S. It is interesting to note the presence of chloride, probably at low levels, in the oxide film, suggesting

Table 7. *The Oxide Composition Deduced from the Main Elements of the Surface of Al-Si9-Cu3 and Al-Si7-Mg0.3 Samples Before and After Immersion for 1 month in the Adriatic Sea*[(A)]

	Before Immersion		After Immersion	
Elements	**Composition (at%)**	**Ratio**	**Composition (at%)**	**Ratio**
	Al-Si9-Cu3			
Al	29.4 (88.3)	(Al/Mg = 26.7) (Al/Si = 10.5)	14.1 (52)	(Al/Mg = 2) (Al/Si = 2.4)
Mg	1.1 (3.3)		7.2 (26.6)	
Si	2.8 (8.4)		5.8 (21.4)	
O	66.7 (0)		72.9 (0)	
	Al-Si7-Mg0.3			
Al	32.3 (89.5)	(Al/Mg = 21.8) (Al/Si = 14)	18.0 (78.3)	(Al/Mg = 9.5) (Al/Si = 5.8)
Mg	1.5 (4.1)		1.9 (8.2)	
Si	2.3 (6.4)		3.1 (13.5)	
O	63.9 (0)		77.0 (0)	

[(A)] The composition was deduced with or without considering oxygen content. Cationic fractions (oxygen content not considered) are given in parenthesis. Ratios Al/Si and Al/Mg are given for cationic fractions only. XPS high-energy resolution and survey spectra are presented in Figures 15, 17, and S8 through S11.

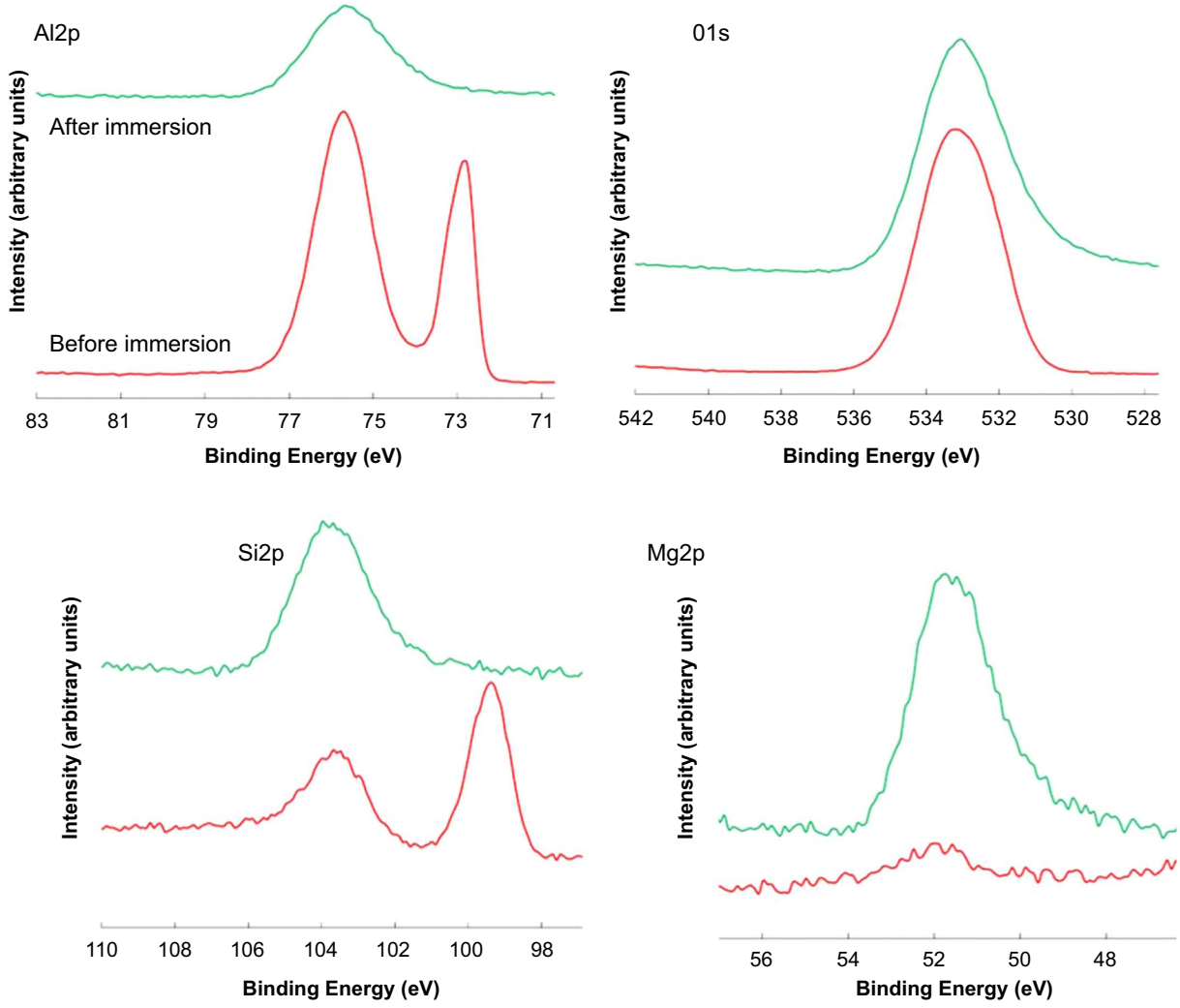

FIGURE 15. *XPS high-resolution spectra recorded at the surface of the Al-Si9-Cu3 samples before and after immersion for 1 month in the Adriatic Sea. The composition is presented in Table 7. The sample was sonicated before the analysis.*

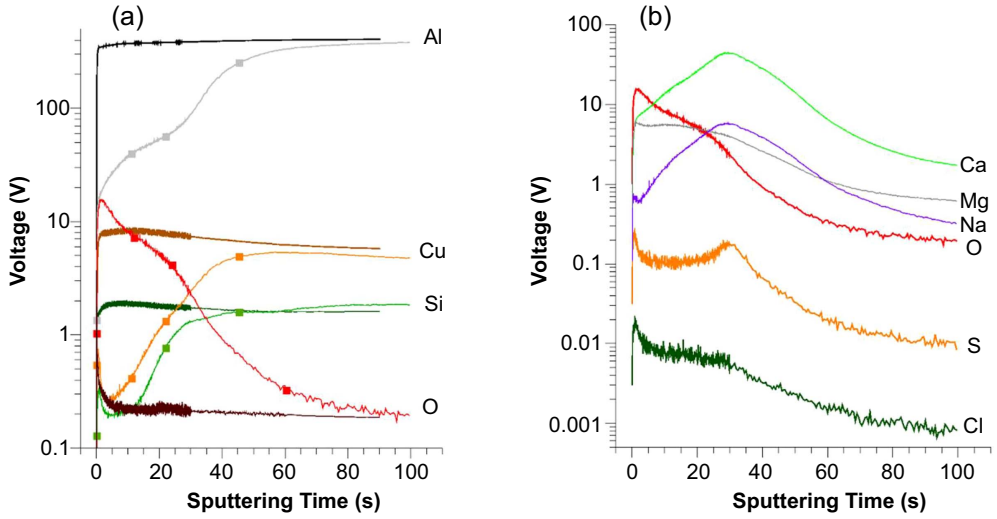

FIGURE 16. *(a) GDOES depth profiles of elements constituting the Al-Si9-Cu3 samples recorded before (line) and after immersion (line + square) in seawater. (b) GDOES depth profiles of elements of the modified layer formed at the surface of the Al-Si9-Cu3 alloy immersed in seawater.*

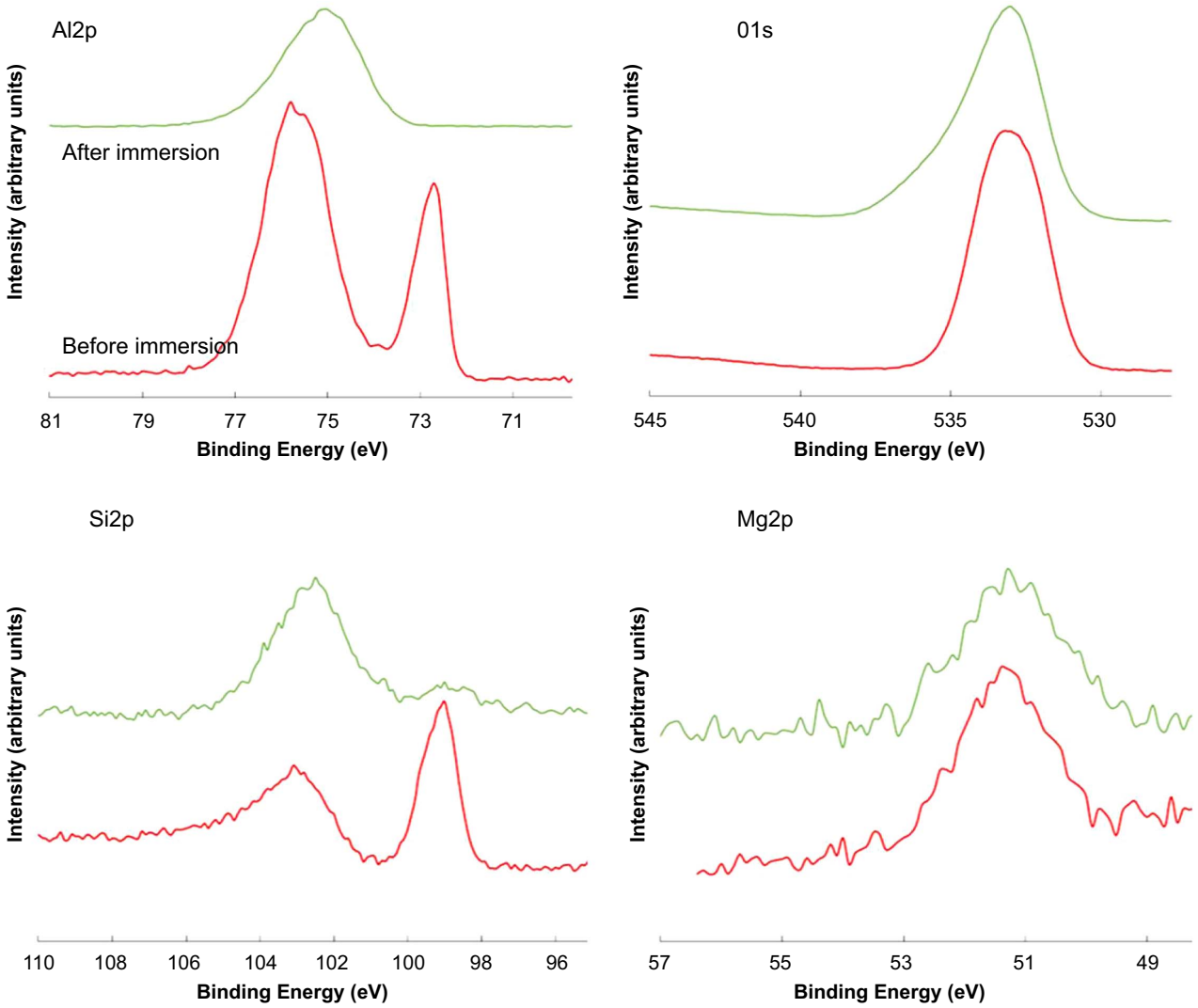

FIGURE 17. *XPS high-resolution spectra recorded at the surface of the Al-Si7-Mg0.3 sample before and after immersion for 1 month in the Adriatic Sea. The composition is presented in Table 7. The sample was sonicated before the analysis.*

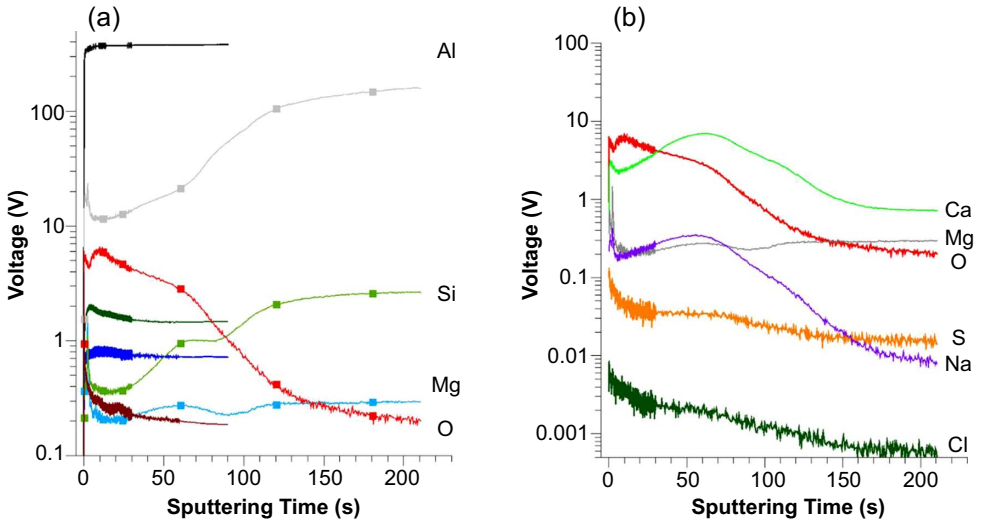

FIGURE 18. *(a) GDOES depth profiles of elements constituting the Al-Si7-Mg0.3 samples recorded before (line) and after immersion (line + square) in seawater. (b) GDOES depth profiles of elements of the modified layer formed at the surface of the Al-Si7-Mg0.3 sample immersed in seawater.*

that the interfacial layer blocks the penetration the chlorides. The evolution of the Mg signal shows enrichment of Mg in the oxide layer, confirming the results of EDS and XPS analyses. Magnesium follows the same trend as chlorides, but it is difficult to define whether magnesium comes from bulk or seawater.

3.4.2 | Al-Si7-Mg0.3 Alloy

The composition of the surface of the nonimmersed and immersed Al-Si7-Mg0.3 sample is presented in Table 7. High-resolution spectra of the main elements are presented in Figure 17; survey and high-resolution spectra of minor elements are presented in Figures S10 and S11, respectively.

The surface of the nonimmersed sample is covered by a naturally formed oxide layer containing mainly Al oxide (Al/Si = 14 and Al/Mg = 21.8). Components associated with Al metal, Al(III) oxide, Si metal, Si(IV) oxide, and Mg(II) oxide are observed at the same binding energies as on the Al-Si9-Cu3 sample (Figure 15). The thickness of 3.4 nm of the oxide layer is calculated from Al metal and Al(III) peaks.

After immersion, the Al signal is much less intense and exhibits only a single peak related to Al(III) oxide. Similarly, a single Si(IV) oxide is present. Compared to the layer formed on Al-Si9-Cu3, the most considerable change occurs for Mg. Namely, Mg was highly enriched in the layer on Al-Si9-Cu3, but only two-fold enrichment was observed for Al-Si7-Mg0.3 (Table 7, Figure 17). The ratio of Al/Si after immersion is 5.8, and that of Al/Mg is 9.5.

XPS results were complemented with GDOES results. As for the AlSiCu alloy, GDOES profiling was performed before and after immersion in seawater under the same conditions (Figure 18). Evolution observed before immersion shows a fast stabilization of Al, Mg, and Si signals, indicating that the bulk has been reached. The fast O decrease indicates that the oxide layer is very thin and corresponds to a native oxide. After immersion, profiles are also strongly modified, indicating an action of the seawater. As for the Al-Si9-Cu3 alloy, a thin oxide layer has grown at the surface of the alloy. The evolution of Al, Si, and Mg signals suggests that this oxide is mainly composed of Al; a similar profile was observed for Si. The sputtering time, which is longer than for the Al-Si9-Cu3 alloy, indicates that the oxide layer is thicker on Al-Si7-Mg0.3, as shown by SEM cross-section analysis (Figure 11).

After 130 s, signals of the alloy elements (Al, Si, and Mg) slowly increased but never reached the bulk levels. This observation may suggest the presence of a strongly roughened interface that the corrosion process in seawater may generate.

As for the Al-Si-Cu alloy, Figure 18(b) shows the presence of two distinct domains, the first corresponding to the oxide and the second to an interfacial zone enriched in Ca and Na. Chlorides seem to be present mainly in the oxide layer, unlike magnesium, which is slightly present in the oxide and shows no peak with maximum as in the case of Al-Si9-Cu3. The measured levels of Ca and Na are lower than for Al-Si9-Cu3 alloy (around 9 V for Ca and 0.4 V for Na for Al-Si7-Mg0.3 and 60 V for Ca and 7 V for Na for Al-Si9-Cu3), indicating that this layer is much less enriched. It seems possible to correlate the enrichment of this layer with the thickness of the oxide formed in the seawater.

3.5 | Electrochemical Measurements Before and After Immersion in Seawater

3.5.1 | Al-Si9-Cu3 Alloy

The polarization curve recorded for bare Al-Si9-Cu3 in artificial seawater is presented in Figure 19(a). The cathodic curve is plateau-shaped over several 100 mV reaching the corrosion potential at E_{corr} = −0.61 V (Table 8). The corrosion current density was 2.97 μA/cm^2. In the anodic cycle, the current density increased with progressing potential due to localized corrosion.

The curves recorded in artificial seawater for samples immersed in the Adriatic Sea for 1, 3, and 8 months are presented in Figure 19(a). The cathodic current density and j_{corr} increased with E_{corr} shifting somewhat positively (Table 8). In the anodic range, however, the increase in current density significantly slowed down, forming a pseudo-passive range, where the current density is not entirely independent of potential, but the increase is considerably diminished. At ca. −0.45 V, the passivity breakdown took place. The curve recorded after 3 and 8 months of immersion were similar to that after 1 month.

The electrochemical response of Al-Si9-Cu3 samples immersed in the Adriatic Sea indicates that the immersion does not significantly deteriorate the surface but rather contributes to its passivation: the electrochemical parameters remained

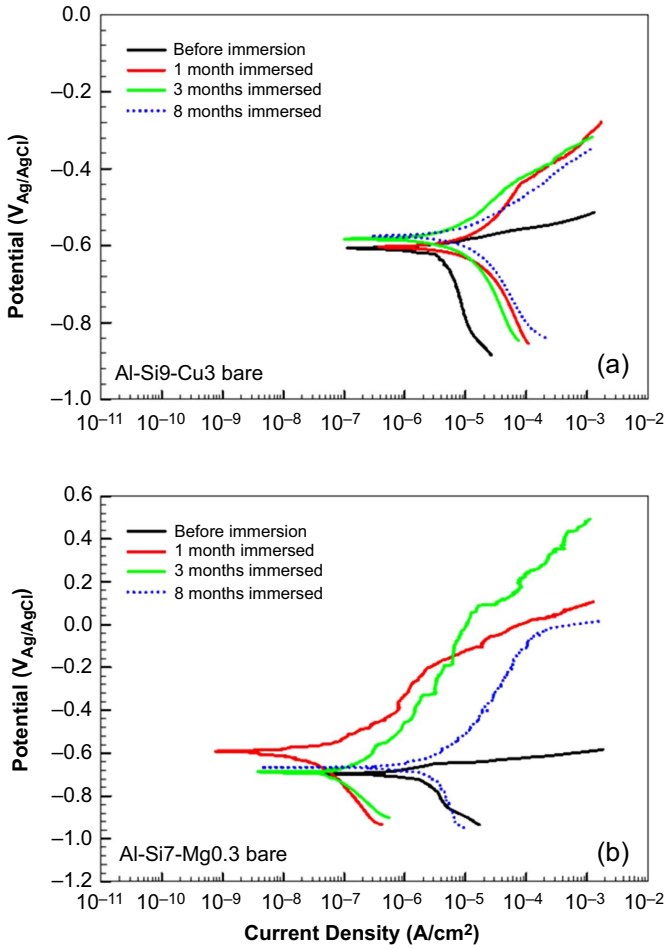

FIGURE 19. *Potentiodynamic polarization curves recorded in artificial seawater for (a) Al-Si9-Cu3 and (b) Al-Si7-Mg0.3 samples before immersion in the Adriatic Sea and after 1, 3, and 8 months of immersion. Before electrochemical measurements, the samples were sonicated to remove the biofilm formed during immersion. For the samples immersed for 8 months, it was difficult to find an area free of biofouling (Figure 7) sufficient to perform the measurements, so dotted lines presented these curves. Note that the y scale differs for (a) and (b). The electrochemical parameters deduced from potentiodynamic curves are presented in Table 8.*

similar to that of nonimmersed alloy, but the narrow passive range was established up to −0.45 V. Therefore, the mixed Al-Mg-Si oxide identified by SEM/EDS, XPS, and GDOES (Figures 10, 15, and 16) is protective. After 8 months of immersion, the j_{corr} values increased from 2.97 μA/cm^2 to 9.98 μA/cm^2 (Table 8). However, compared to the nonimmersed sample, the increase of

Table 8. *The Electrochemical Parameters Deduced from the Potentiodynamic Polarization Curves (Figure 19) Recorded for Al-Si9-Cu3 and Al-Si7-Mg0.3 Samples Before and After Immersion for 1, 3, and 8 months in the Adriatic Sea*[(A)]

Condition	E_{corr} (V)	j_{corr} (μA/cm^2)	R_p (kΩ·cm^2)	E_{br}/V (ΔE/mV)
Al-Si9-Cu3				
Before immersion	−0.61±0.02	2.97±0.24	3.5±1.6	−0.62 V (10 mV)
1 month immersed	−0.59±0.01	5.23±1.40	3.0±0.7	−0.44 V (150 mV)
3 months immersed	−0.56±0.01	2.77±0.51	3.0±0.1	−0.43 V (130 mV)
8 months immersed	*−0.57±0.02*	*9.98±0.51*	*2.0±0.1*	*−0.38 V (190 mV)*
Al-Si7-Mg0.3				
Before immersion	−0.69±0.01	1.06±0.03	16±1	−0.65 V (40 mV)
1 month immersed	−0.58±0.04	0.03±0.01	198±29	−0.005 V (575 mV)
3 months immersed	−0.67±0.05	0.07±0.02	411±143	0.09 V (760 mV)
8 months immersed	*−0.66*	*2.57*	*19*	*−0.003 V (657 mV)*

[(A)] The samples were sonicated before the analysis. For the samples immersed for 8 months, it was for several samples, difficult to find an area free of biofouling (values written in italics).

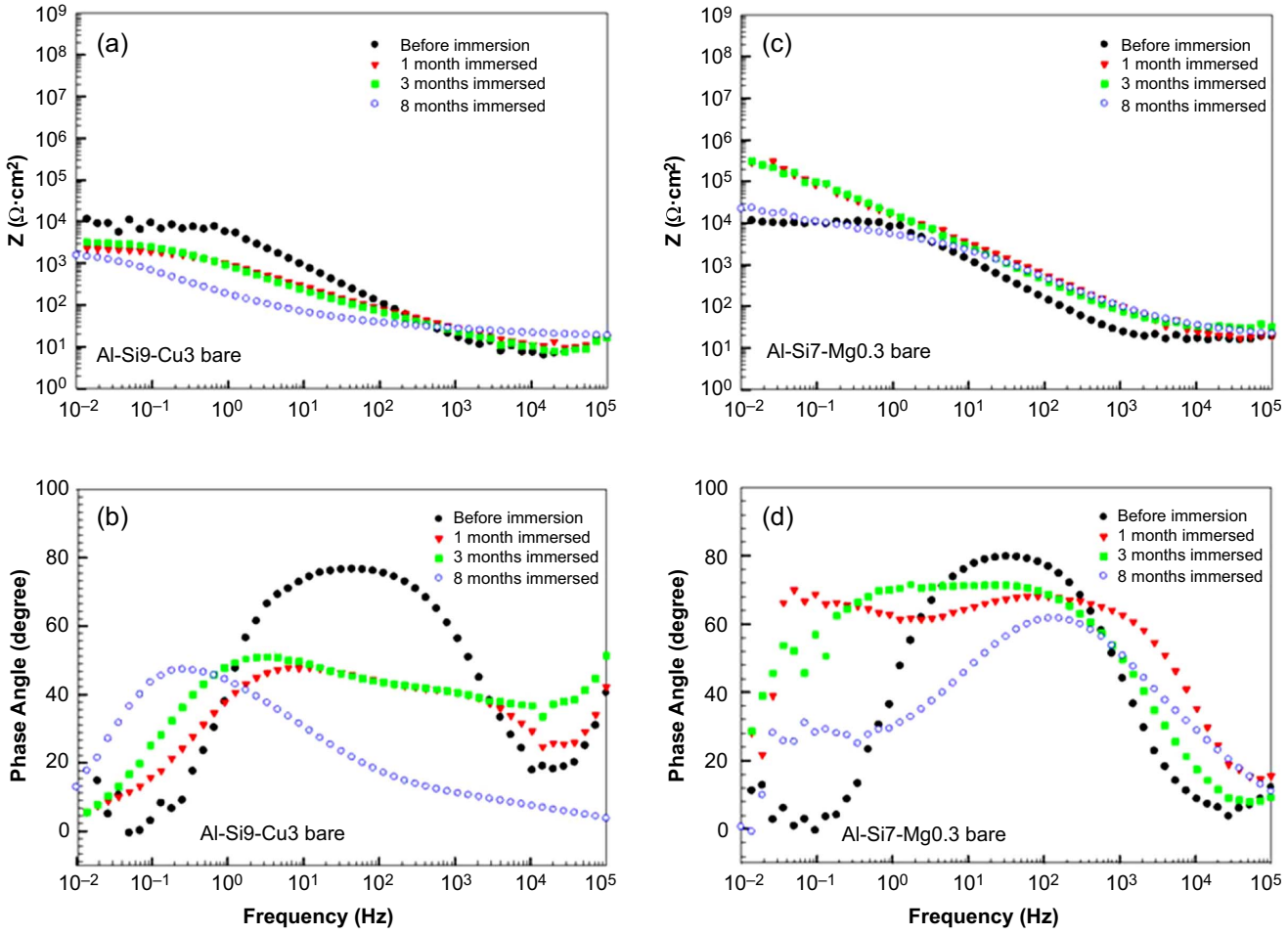

FIGURE 20. *Bode plots of (a, c) impedance magnitude and (b, d) phase angle as a function of frequency recorded in artificial seawater for (a, b) Al-Si9-Cu3 and (c, d) Al-Si7-Mg0.3 samples before immersion in the Adriatic Sea and after 1, 3, and 8 months immersion. Before electrochemical measurements, the samples were sonicated to remove the biofilm formed during immersion. For the samples immersed for 8 months, it was difficult to find an area free of biofouling sufficient to perform three replicates; blue circles presented these curves.*

the anodic branch is significantly slower, confirming that the surface layer formed during immersion is still protective.

EIS measurements performed at the open-circuit potential are presented in Figures 20(a) and (b). Following the linear increase in the mid frequencies (f), an impedance magnitude (|Z|) plateau with |Z| at 10^4 Ω·cm^2 was established between f of 1 Hz and 10^{-2} Hz. Phase angle (φ) plot vs. f shows a plateau at −80° in the f range from 10^2 Hz to ca. 5 Hz. At smaller frequencies, φ decreased. This feature shows that a layer with some capacitive character was formed. After immersion in the Adriatic Sea, the curves remained similar, but the increase in |Z| with f in the mid-range was slowed down with |Z| reaching smaller values at the lowest f, i.e., ca. 2×10^3 Ω·cm^2, than before immersion.

3.5.2 | Al-Si7-Mg0.3 Alloy

The polarization curve recorded for bare Al-Si7-Mg0.3 in artificial seawater is presented in Figure 19(b). This alloy exhibits more negative E_{corr}, smaller j_{corr}, and higher R_p than the Al-Si9-Cu3 alloy (Table 8). In the course of immersion in seawater, these two alloys differ significantly. The passive layer formed on Al-Si7-Mg0.3 developed a broad passive region over 3 months of immersion, resulting in a 15-fold decrease in j_{corr} and a 26-fold increase in R_p. Moreover, a broad passive range of over 700 mV was established. The curve recorded after 8 months of immersion showed the deterioration of electrochemical passivity compared to after 3 months but still much better than that of nonimmersed alloy. The passive range was broad, over 600 mV, indicating that the surface oxide layer still assured a high level of protection of the underlying substrate.

EIS data in Figures 20(c) and (d) corroborated potentiodynamic data. The impedance plot before immersion is similar to that of Al-Si9-Cu3, but with immersion, the impedance increased, showing a broad range of frequencies where the layer with capacitive character is formed. After 3 months of immersion, impedance magnitude at the lowest frequency was higher for Al-Si7-Mg0.3 than for Al-Si9-Cu3. After 8 months, the impedance decreased for the latter as well.

CONCLUSIONS

Two cast aluminum-silicon alloys were investigated for marine applications by field immersion testing in the Adriatic Sea. Before and after immersion, the samples were investigated using surface analytical techniques (FIB-SEM/EDS, XPS, and GDOES) to characterize microstructure and composition. Further, electrochemical measurements in artificial seawater were conducted to account for long-term corrosion properties. Biofouling was noted during immersion.

➢ Al-Si9-Cu3 alloy comprises α-Al-rich matrix, eutectic Si grains, and various Al-Si-Fe(Mn,Cu,Mg) IMPs. Al-Si7-Mg0.3 alloy comprises α-Al-rich matrix, larger eutectic areas, and a smaller number of intermetallics than Al-Si9-Cu3.

➢ During immersion in the Adriatic Sea, the biofouling was progressively formed, first as micro- and then as macrobiofoul. After 1 month of immersion, biofoul could be almost completely removed by sonication (simulating removal due to vessel in motion). At more prolonged immersion, sonication could not entirely remove the macro biofoul, e.g., diatoms.

➢ After 1 month of immersion, a micrometer thick oxide layer was formed on the Al-Si9-Cu3 alloy. EDS, XPS, and GDOES analyses confirmed that this layer was rich in Mg, probably incorporated from seawater. The protective oxide layer ensured that the electrochemical parameters did not deteriorate during immersion. A passive range of 110 mV to 140 mV was established.

➢ On Al-Si7-Mg0.3 alloy, two distinct regions were formed during immersion: Al-oxide was formed on the matrix with small amounts of Mg and Si; on the eutectic region, an Al-oxide rich in Si grains developed. This part contained doubled concentration of Si compared to the underlying alloy. The oxide layer formed on Al-Si7-Mg0.3 alloy during immersion in the Adriatic Sea showed better passivation behavior than Al-Si9-Cu3, which improved up to 3 months of immersion, showing the extent of the passive region of over 700 mV.

➢ Cast aluminum-silicon alloys are suitable for marine applications, especially alloys containing magnesium (EN AC 42100).

ACKNOWLEDGMENTS

This work is a part of the M-ERA.NET project entitled "*Design of corrosion resistant coatings targeted for versatile applications*" (acronym COR_ID). The financial support of the project by MESS (Ministry of Education, Science, and Sport of the Republic of Slovenia) and ANR (The French National Research Agency) is acknowledged. This work is also a part of the bilateral Proteus program between Slovenia and France entitled "DCOIN: Disentangling COrrosion and its INhibition" and INCOR: INterfaces relevant for CORrosion and its inhibition", financed by the Slovenian Research Agency (SRA) and the ANR (Grant No. BI-FR/21-22-008). The financial support from the SRA (research core funding No. P2-0393 and P1-0134) is acknowledged. Région Ile-de-France is acknowledged for partial funding of the XPS equipment. The authors acknowledge the Centre of Excellence in Nanoscience and Nanotechnology—Nanocenter (CENN), Ljubljana, Slovenia, to access the scientific equipment (FIB-SEM/EDS). The authors acknowledge D. Zimerl, G. Šekularac, D. Hamulić, and U. Tiringer for valuable technical help and Prof. A. Cör and Dr. K. Šuster for valuable discussions. The authors also thank co-workers of the Marine Biology Station of the National Institute of Biology in Piran, Slovenia: Dr. A. Ramšak for the expert discussion, Dr. V. Malačič for providing data from the Vida buoy and diver T. Makovec for handling the samples and recording the video material in the Supplemental Material. The company Talum d. d. Tovarna aluminija Kidričevo, Slovenija, is acknowledged for production and providing the cast Al-Si alloys.

References

1. J.R. Davis, ed., *Corrosion of Aluminum and Aluminum Alloys* (Materials Park, OH: ASM International, 2000).
2. M.A. Wahid, A.N. Siddiquee, Z.A. Khan, *Mar. Syst. Ocean Technol.* 15 (2020): p. 70-80.
3. N.J.H. Holroyd, G.M. Scamans, *Corrosion* 72 (2016): p. 136-143.
4. K. Nişancioğlu "Corrosion and Protection of Aluminium Alloys in Seawater," in *Corrosion Behaviour and Protection of Copper and Aluminium Alloys in Seawater*, ed. D. Féron (Cambridge, England: Woodhead Publishing Ltd.: CRC Press, 2007).
5. https://www.factmr.com/report/aluminium-alloys-market.
6. C. Berlanga-Labari, M.V. Biezma-Moraleda, P.J. Rivero, *Metals* 10 (2020): p. 1384.
7. "Aluminium and the Sea", Alcan Marine, http://www.ansatt.hig.no/henningj/materialteknologi/lvd-aluminium%20and%20the%20sea.htm.
8. J.R. Murray, A.J. McAllister, *Bull. Alloy Phase Diagr.* 5, 1 (1984).
9. M. Haghshenas, J. Jamali, *Case Stud. Eng. Fail. Anal.* 8 (2017): p. 11-20.
10. M. Yildirim, D. Özyürek, *Mater. Des.* 51 (2013): p. 767-774.
11. D. Stanić, Z. Zovko Brodarac, L. Li, *Metals* 10 (2020): p. 1623.
12. M.V. Kral, *Mater. Lett.* 59 (2005): p. 2271-2276.

13. J.A. Taylor, *Proc. Mater. Sci.* 1 (2012): p. 19-33.
14. E. Cerrri, M.T. Di Giovanni, E. Ghio, *La Metall. Italiana* (2020): p. 37-47.
15. D.J. Chakrabarti, D.E. Laughlin, *Prog. Mater. Sci.* 49 (2004): p. 389-410.
16. C. Cayron, P.A. Buffat, *Acta Mater.* 48 (2000): p. 2639-2653.
17. M.L.C. Lim, J.R. Scully, R.G. Kelly, *Corrosion* 69 (2013): p. 35-47.
18. G.M. Scamans, N.J.H. Holroyd, C.D.S. Tuck, *Corros. Sci.* 27 (1987): p. 329-347.
19. W.R. Osório, P.R. Goulart, A. Garcia, *Mater. Lett.* 62 (2008): p. 365-369.
20. W.R. Osório, N. Cheung, J.E. Spinelli, P.R. Goulart, A. Garcia, *J. Solid State Electrochem.* 11 (2007): p. 1421-1427.
21. M.A. Pech-Canul, M.I. Pech-Canul, P. Bartolo-Pérez, M. Echeverría, *Electrochim. Acta* 140 (2014): p. 258-265.
22. M. Eslami, F. Deflorian, C. Zanella, *C*orrosion 75 (2019): p. 1339-1353.
23. S. Smokvina-Hanza, L. Vrsalović, L. Štic, L. Liverić, *Eng. Rev.* 41 (2021): p. 115-123.
24. J. Ščepanović, V. Asanović, D. Radonjić, D. Vuksanović, S. Herenda, F. Korać, F. Bikić, *J. Serb. Chem. Soc.* 84 (2019): p. 1-14.
25. A.M. Cardinale, D. Macciò, G. Luciano, E. Canepa, P. Traverso, *J. Alloys Compd.* 695 (2017): p. 2180-2189.
26. G. Šekularac, J. Kovač, I. Milošev, *Corros. Sci.* 169 (2020): p. 108615.
27. G. Šekularac, I. Milošev, *J. Electrochem. Soc.* 167 (2020): p. 021509.
28. G. Šekularac, J. Kovač, I. Milošev, *J. Electrochem. Soc.* 167 (2020): p. 111506.
29. G. Šekularac, I. Milošev, *Corros. Sci.* 144 (2018): p. 54-73.
30. E. Gardin, S. Zanna, A. Seyeux, D. Mercier, A. Allion-Maurer, P. Marcus, *Biointerphases* 15 (2020): p. 041014.
31. S. Zanna, A. Seyeux, A. Allion-Maurer, P. Marcus, *Corros. Sci.* 175 (2020): p. 108872.
32. I. Milošev, P. Rodič, B. Kapun, C. Carrière, D. Mercier, S. Zanna, P. Marcus, *Corrosion* 79, 2 (2023): p. 213-229.
33. I. Vilibić, P. Zemunik, J. Šepić, N. Dunić, O. Marzouk, H. Mihanović, C. Denamiel, R. Precall, T. Djakovac, *Ocean. Sci.* 15 (2019): p. 1351-1362.
34. S. Al. Shehadat, M. O. Gorduysus, S. S. Abdul Hamid, N. A. Abdullah, A. R. Samsudin, A. Ahmad, *Eur. J. Dent.* 12 (2018): p. 574-578.
35. J.H. Scofield, *J. Electron Spectrsc. Relat. Phenom.* 8 (1976): p. 129-137.
36. S. Tanuma, C.J. Powell, D.R. Penn, *Surf. Interface Anal.* 17 (1991): p. 911-926.
37. J.P. Bidwell, S. Spotte, *Simulated Seawater: Formulas and Methods* (Boston, MA: Jones and Bartlett Publishers, 1985).
38. E. McCafferty, *Introduction to Corrosion Science* (New York, NY: Springer Science & Business Media, 2010).
39. M.M. Buarzaiga, S.J. Thorpe, *Corrosion* 50 (1994): p. 176-185.
40. R. Arrabal, B. Mingo, A. Pardo, M. Mohedano, E. Matykina, I. Rodríguez, *Corros. Sci.* 73 (2013): p. 342-355.
41. S.J. Brooks, M. Waldock, "Copper Biocides in the Marine Environment," in *Ecotoxicology of Antifouling Biocides*, eds. T. Arai, H. Harino, M. Ohji, W.J. Langston (New York, NY: Springer, 2009), p. 413-428.
42. https://srdata.nist.gov/xps.
43. I. Milošev, H.H. Strehblow, *J. Electrochem. Soc.* 150 (2003): p. B517-B524.